Draft version October 14, 2020
Typeset using LaTeX default style in AASTeX63

Exploring Super-Earth Surfaces: Albedo of Near-Airless Magma Ocean Planets and Topography

Darius Modirrousta-Galian,[1,2] Yuichi Ito,[3] and Giuseppina Micela[1]

[1] *INAF – Osservatorio Astronomico di Palermo, Piazza del Parlamento 1, I-90134 Palermo, Italy*
[2] *University of Palermo, Department of Physics and Chemistry, Via Archirafi 36, Palermo, Italy*
[3] *Department of Physics & Astronomy, University College London, Gower Street, WC1E 6BT London, United Kingdom*

(Accepted)

Submitted to Icarus

ABSTRACT

In this paper we propose an analytic function for the spherical albedo values of airless and near-airless magma ocean planets (AMOPs). We generated 2-D fractal surfaces with varying compositions onto which we individually threw 10,000 light rays. Using an approximate form of the Fresnel equations we measured how much of the incident light was reflected. Having repeated this algorithm on varying surface roughnesses we find the spherical albedo as a function of the Hurst exponent, the geochemical composition of the magma, and the wavelength. As a proof of concept, we used our model on Kepler-10b to demonstrate the applicability of our approach. We present the spherical albedo values produced from different lava compositions and multiple tests that can be applied to observational data in order to determine their characteristics. Currently, there is a strong degeneracy in the surface composition of AMOPs due to the large uncertainties in their measured spherical albedos. In spite of this, when applied to Kepler-10b we show that its high albedo could be caused by a moderately wavy ocean that is rich in oxidised metallic species such as FeO, Fe_2O_3, Fe_3O_4. This would imply that Kepler-10b is a coreless or near-coreless body.

Keywords: Extra-solar planets — Terrestrial planets — Volcanism — Interiors — Spectrophotometry

1. INTRODUCTION

The inferred high spherical albedo values of several hot super-Earths (Demory 2014; Malavolta 2018) are well above what the current literature predicts for magmatic surfaces (Essack et al. 2020; Rouan et al. 2011; Edgett and Rice 1997). Two main explanations have been put forward: reflective exotic magmas (Rouan et al. 2011) and reflective volcanic/mineral atmospheres (Hamano et al. 2015; Pluriel et al. 2019). However, it is currently not possible to verify which mechanism applies to specific super-Earths due to observational data being either limited or degenerate. Generally, constraining the properties of super-Earth exoplanets is troublesome due to their small sizes (Valencia et al. 2013; Dorn et al. 2017). In spite of this, advances in mass-radius measurements and superior spectroscopic analyses of their atmospheres (e.g. Tsiaras et al. 2016; Esteves et al. 2017) has lowered their compositional degeneracies. These advancements have permitted researchers to apply geological models to specific super-Earths in order to better understand their structures (e.g. Zeng and Sasselov 2013; Zeng et al. 2016, 2018). However, one aspect that remains unexplored is the surface composition and topology of these bodies. Directly analysing the geomorphology of extra-solar planets is not possible due to the observational limitations set by the *Rayleigh Criterion*. For example, if one wanted to resolve a feature that occupies 10% of a planetary surface (e.g. an ocean) on an Earth-sized exoplanet located 5 pc away, a spatial resolution of a few microarcseconds would be required. However, this is beyond our present capabilities which is one of the reasons why it is troublesome to decipher which mechanisms lead to large albedos on molten super-Earths such as Kepler-10b, Kepler-21b and K2-141b (Rouan et al. 2011; Demory 2014; Malavolta 2018).

Corresponding author: Darius Modirrousta-Galian
darius.modirrousta@inaf.it

The purpose of our study is to investigate the spherical albedo values of airless and near-airless, molten super-Earths with a particular focus on its dependence to the composition and ocean waviness. As this study is a first stepping-stone to theoretically estimate the albedo of these ultra-hot exoplanets, we had to set some simplifications (see Sec. 5.5) and left some tasks for future works (see Sec. 5.6). We show that the ocean's roughness will lead to a higher degeneracy in the interpretation of the spherical albedo values of these systems. The close-orbiting super-Earths relevant to our study will be tidally locked therefore containing a molten day-side and a cold night-side. Due to the high day-side temperatures, a vaporised mineral atmosphere will form that rapidly traverses into the night-side where the temperatures are low enough for the minerals to condense (Schaefer et al. 2012; Ito et al. 2015; Kite et al. 2016). Whilst the atmosphere is expected to be generally optically thin in most of the infrared spectral range, the rapidly expanding gas would carry enough kinetic energy to trigger magma ocean waves (see Sec. C of the appendix and Kite et al. (2016)). In Sec. 2 we justify our choice of using Kepler-10b as an analogue planet for our spherical albedo model. In Sec. 3.1 we model the magma ocean waves using fractal mathematics. In Sec. 3.2 we explain that while mineral atmospheres may affect the spherical albedo values within the spectral range of the *Kepler* telescope, for future missions with larger wavelength ranges, the effects would be negligible. In Sec. 4 we show the results of our simulations and we present an analytic approximation for the planar albedo, which we then integrate across all angles to determine the spherical albedo. Our analytic functions model the spherical albedo values of molten, airless magma ocean super-Earths for different roughnesses and surface compositions. Finally, in Sec. 5 and 6 we discuss and present our results respectively.

Note that many of the terms used within this manuscript to describe the reflective properties of super-Earths are similar but not identical so it is necessary to define them to avoid confusion. The reflectance, R, is a directional quantity that depends on the incident and emerging angles, as well as the wavelength of the light and the composition (via the refractive indices) and roughness of the surface. The spherical albedo, A_S, is the total fraction of incident radiance scattered by a body into all direction. The planar (or plane) albedo, A_{pla}, is the spherical albedo of a planar surface of the planet. Finally, the bolometric Bond albedo, A_B, is the spherical albedo integrated across all wavelengths.

2. OUR CHOICE OF PLANET

Throughout the rest of this manuscript we will use Kepler-10b as an analogue for molten, airless super-Earths within our spherical albedo models. We do this for two reasons: first we want to input realistic parameters into our simulations instead of speculative idealised ones. Secondly, we want to show how our analytic function for the spherical albedo values can be applied with ease to any molten, airless super-Earth of choice. Therefore, before we progress into an explanation of our models we would first like to justify our choice of using Kepler-10b as our test planet. We believe this body is an adequate candidate for our method because most mass and radius measurements are consistent with a rocky composition (e.g. Batalha et al. 2011; Fogtmann-Schulz et al. 2014; Dumusque et al. 2014; Esteves et al. 2015; Weiss et al. 2016; Dai et al. 2019, see Fig. 1). Furthermore, the strong temperature contrast inferred from the observed phase curve between the day-side temperature of $\simeq 2750$ K and night-side temperature $\simeq 50$ K implies that a thick atmosphere is improbable (Rouan et al. 2011). In addition, the large thermal gradient is suggestive that Kepler-10b is tidally locked. Hence, the vaporised mineral gases formed on the day-side (Schaefer et al. 2012; Ito et al. 2015) will rapidly expand into the night-side and condense, forming waves in the magma ocean beneath as they travel (Kite et al. 2016). Whilst there is still an ambiguity in the measured data, in this paper we focus on the scenario where Kepler-10b is a rocky exoplanet hosting a fully magmatic day-side that is lacking a significant atmosphere. Currently, the best fit value for the bolometric Bond albedo is 0.48 ± 0.35 (Rouan et al. 2011), which is the one we will reference throughout this paper. This study investigates the spherical albedo values for various magma ocean compositions and surface roughnesses. The spherical albedo is useful to consider because it is defined to be a monochromatic property, so it is independent of the irradiation spectrum of the host star. From our spherical albedo values and an estimation of the stellar spectra, the bolometric Bond albedo values could be inferred (see Marley et al. 1999, for an example of a similar concept but for planets with atmospheres). It is also important to note that the primary objective of this study is to present our model for constraining the composition of exoplanetary magma oceans; we are therefore not focusing on formational or observational limitations.

3. MODELS

3.1. *Generating our Magma Ocean Fractal Surfaces*

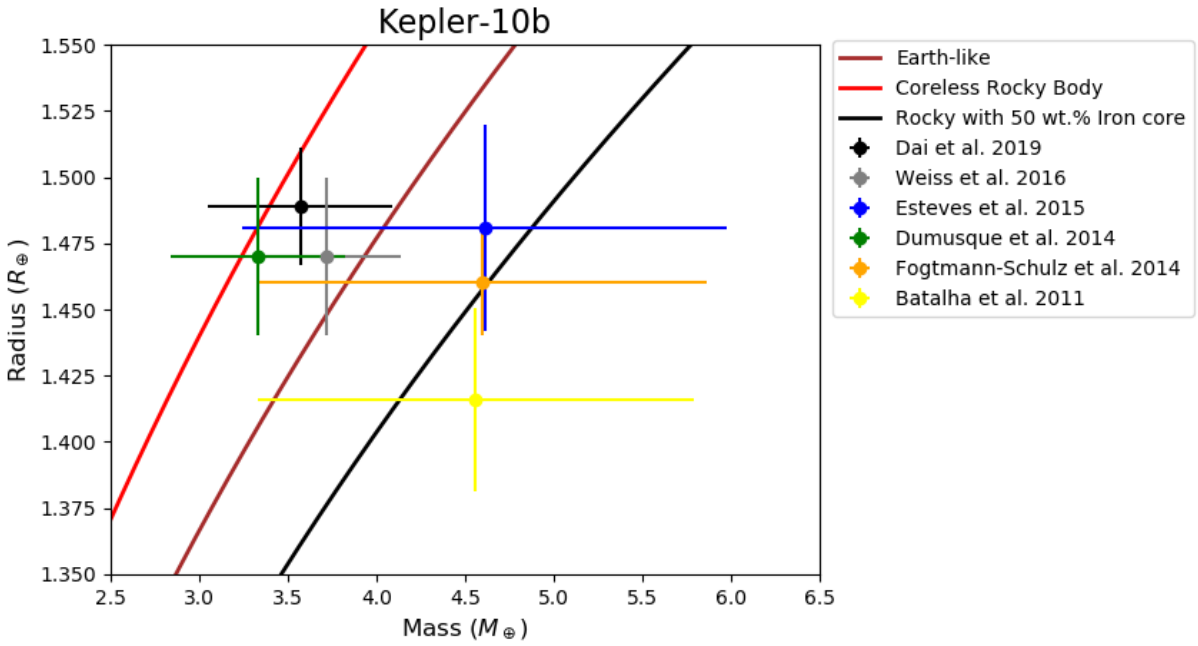

Figure 1. The mass and radius of Kepler-10b according to different studies. The planetary composition model curves are from Zeng and Sasselov (2013) and Zeng et al. (2016). The variations in the measurements are due to a combination of uncertainties in the stellar parameters and using different observational raw data.

One commonly used, although incomplete, definition of a fractal was given by Benoit Mandelbrot as a shape whose fractal dimension (also called Hausdorff dimension) is greater than its topological dimension. The fractal dimension is a measure of the geometric complexity of a system so that from a geological perspective, this parameter would provide information on the roughness of a surface. For instance, Earth's oceans have calculated fractal dimensions of ≈ 2.3 (Stiassnie 1991; Stiassnie et al. 1991) which means that due to surface inhomogeneities Earth's true surface area could be several orders of magnitude greater than what is predicted from a perfect spherical model. Similar analyses have also been performed on the fractal-nature of Mars (Deliège et al. 2017; Demin et al. 2017) and Venus (Demin et al. 2018). Roughness has also been shown to affect the reflective properties of non-fluid surfaces with coarser systems having lower ones than their smoother counterparts (e.g. Bennett and Porteus 1961). This is because with a rough surface photons can get trapped in crevices and consequently absorbed. In contrast, with smooth surfaces photons are absorbed less as the albedo values are only dependent on the material properties. For example, soil (Matthias et al. 2000) and ice (Lhermitte et al. 2014) have been found to be almost $\sim 50\%$ less reflective than their standard values when they are rough. This is explained by a difference in the phase function of a rough surface and that of a smooth one with the same composition. In addition, several studies have found strong linear relationships between soil's albedo values and its roughness (Oguntunde et al. 2006; Cierniewski et al. 2013). In contrast, when dealing with fluids their bolometric Bond albedo values do not scale proportionally to the roughness of the system (Haltrin et al. 2001). This is because liquid waves are topologically distinct from the types of concavities one would find in solids (e.g. cracks, holes etc.). Waves are not as efficient in trapping photons so other effects such as the angle of incidence of the light ray relative to the immediate surface, and the number of internal reflections are important as they determine how much energy is lost. Since this cannot be modelled analytically, in this paper we perform ray tracing simulations in order to determine the reflective properties of synthetic magma ocean surfaces.

To keep the simulations inexpensive we will use Schlick's approximation, Eq. 1a, for the reflectance at a liquid boundary (Schlick 1994). Schlick's approximation is not an exact solution, but rather a method of keeping the ray tracing simulations inexpensive, whilst still maintaining physical accuracy. This method only works when the ray of light is traversing from a medium with a low refractive index to that of a higher one, which is relevant to our model. We are aware that this approximation will inevitably result in a decrease of accuracy but we unfortunately had to

make this compromise in order to cover the large parameter space within a reasonable time-frame. In Sec. A of the appendix we compare Schlick's approximation with other models and the exact Fresnel equations in order to quantify their differences. We define the parameter n_{sy} as the synthetic refractive index of the magma, which accounts for the effects of the real (n) and imaginary (k) indices. The derivation of the synthetic refractive index, n_{sy}, is shown in Sec. B of the appendix. Therefore, n_{sy} is dependent on the geochemical composition of the medium and the wavelength of the light as shown by the best-fit equations listed in Table 5:

$$R(\theta) \approx R_0 + (1 - R_0)(1 - \cos\theta)^5 \tag{1a}$$

$$R_0 = \left(\frac{n_{sy} - 1}{n_{sy} + 1}\right)^2 \tag{1b}$$

$$n_{sy} = \frac{\left(\frac{|n-1|^2+|k|^2}{|n+1|^2+|k|^2}\right)^{1/2} + 1}{1 - \left(\frac{|n-1|^2+|k|^2}{|n+1|^2+|k|^2}\right)^{1/2}} \tag{1c}$$

Where θ is the angle of incidence and R is the reflectance. Having chosen our equations, the next step was to model the fractal ocean surfaces. We used the *fbm 0.3.0* python package with the Davies and Harte (1987) fractional Gaussian noise (fGn) method. This technique is theoretically exact in generating discretely sampled fGn numerical values for a given fractal dimension. A thorough explanation of the Davies and Harte method can be found in page 412 of Wood and Chan (1994). We chose to model the magma ocean surfaces as a collection of different points with elevations given by fGn in order to approximate the random motions induced from the vapourised atmospheric winds (see Sec. C of the appendix for a mathematical relationship of the wind energies and the surface roughness). However, this approach assumes that each point is independent of its neighbours which would only be true for a zero viscosity fluid (i.e. a superfluid) that also lacks surface tension. Clearly magmas have viscosities so the non-continuous, sharp terrains are unrealistic. Fig. 2 is an example of a pre-smoothed, unrealistic surface. In order to smooth these surfaces we applied a Gaussian filter with a standard deviation of 100 pixels (equivalent to 1 m) given by the *Astropy* package (Astropy Collaboration et al. 2013, 2018). The process of smoothing the surface is analogous to adding a viscosity which, by definition, will act against the fluid flow. We chose to smooth out perturbations smaller than 1 m as this closely matches the waves we observe on Earth's oceans (see Sec. 5.5 for a justification of why the waves of Earth's oceans are an appropriate analogue for the roughness of the magma ocean on Kepler-10b and other ultra-hot super-Earths). From a mathematical perspective, the act of smoothing perturbations smaller than 1 m means that fractal behaviour seizes at very small scales which is expected for natural entities instead of idealised mathematical constructs. It must be noted that maximising the Gaussian filter will produce a smooth surface so that the planar albedo will be given by Eq. 1b. If instead no filter is applied then the planar albedo will converge to 1 as the individual waves will be very thin and tall (i.e. the waves will be steep so the angle θ will approach 90°; see Fig. 2). These two scenarios are unrealistic as they require extreme viscosities which is unlikely given the thermodynamic conditions and magma compositions considered in this study. Concerning with the average wave peak amplitude, this required finding a relationship between the Hurst exponent, which measures the coherence of the surface, and the root mean squared (RMS) roughness. Experimental results from Durst et al. (2011) found that the fractal dimension and the RMS were related by the following equation:

$$RMS \approx h_0 (F - 2) \tag{2}$$

Where h_0 is a height constant and F is the fractal dimension. For self-similar processes where local and global properties are interlinked, the fractal dimension is related to the Hurst exponent by $F = 3 - H$. Therefore H can be substituted in:

$$RMS \approx h_0 (1 - H) \tag{3}$$

We decided to work with the Hurst exponent (H) instead of the fractal dimension (F) in order to make our code easier to adopt. This is because the Hurst exponent is independent of the topological dimension, whilst the fractal dimension is not. Therefore, if one wanted to implement our code into a 1-D, 2-D or 3-D radiative transfer model, the same Hurst exponent could be used resulting in the same spherical albedo value for each scenario. The constant h_0 is calculated experimentally, which can be done using Earth's oceans as an analogue. We know that these have a Hurst

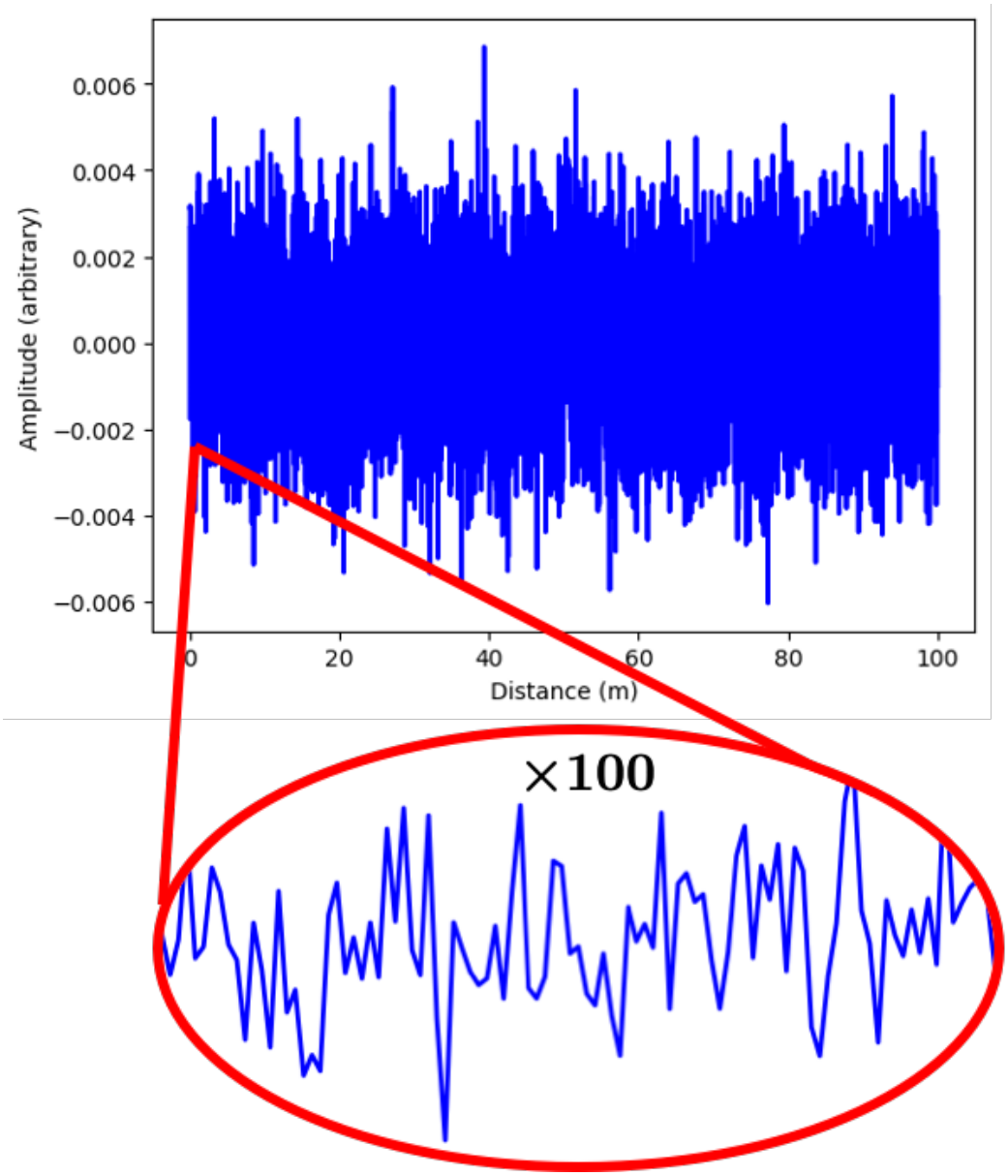

Figure 2. The unsmoothed fractal surface of an ocean whose wave heights are yet to be adjusted for. This surface was generated for a Hurst exponent of 0.7. The circled area is a magnification of a $\times 100$ for the region $0 - 1$ m

exponent of ≈ 0.7 (Stiassnie 1991; Stiassnie et al. 1991) with a root mean squared average waveheight of ≈ 1.5 m (Met Office 2010). Consequently, solving Eq. 3 for $H = 0.7$ and RMS $= 1.5$ m gives $h_0 \approx 5$ m, yielding the final form of our equation:

$$RMS \approx 5\,(1 - H) \tag{4}$$

In order to correct for the height of our magma ocean waves we implemented Eq. 4. This was done by taking the smoothed (i.e. the Gaussian filter had been applied), unadjusted surface and finding the average (absolute) height. The RMS value (calculated with Eq. 4) was then divided by the average height of the smoothed surface to find the average correction factor. Finally, we multiplied the average correction factor to each point in the smoothed, unadjusted surface in order to get our more realistic magma ocean surface as shown by Fig. 3. Note that we are assuming that

the parameter h_0 is constant and equal for the Earth and Kepler-10b. This assumption has been made because the viscosity of magma at very high temperatures is fortuitously similar to that of water. We explain this point more thoroughly in Sec. 5.5.

Once we had the fractal surface generator we created a basic simulator that would throw 10,000 light rays whose initial locations were uniformly sampled. Each of these light rays interacted specularly with the surface according to the approximate Fresnel equations (1a,1b) and the refractive index equations listed in Table 5. By recording how much of the incident light was reflected we constrained the planar albedo of the surfaces for different compositions and roughnesses. We set the boundary condition that if a light ray lost more than 99.99% of its strength we stopped any further interactions and assumed it was fully absorbed. This was done in order to increase the efficiency of our code.

Fig. 3 shows an example of a light ray reflecting specularly on our synthetic smoothed, height-corrected magma oceans surface. The bouncing angles may seem distorted because of the scale difference between the x- and y-axes. Fig. 3 is also a good example of how a light ray may get trapped in a crevice resulting in it bouncing multiple times so a large portion of its original intensity is lost through absorption. With the simulator ready we began taking

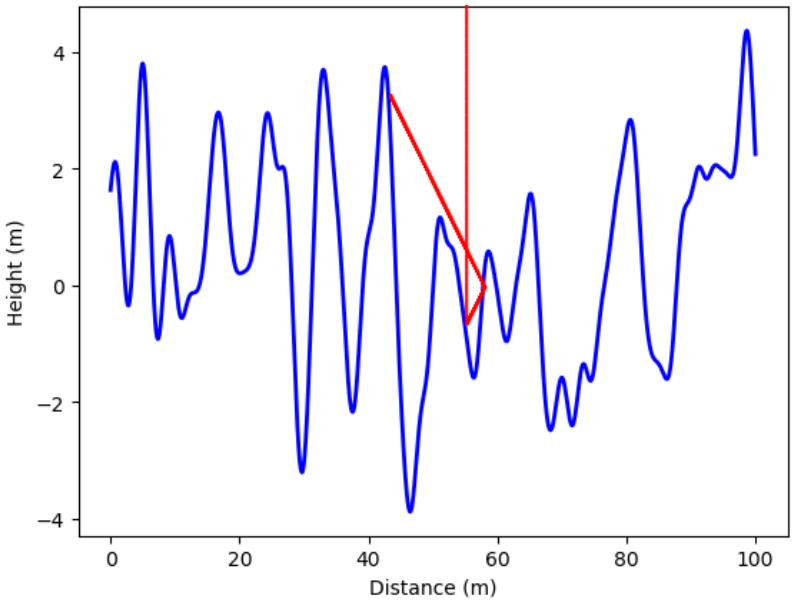

Figure 3. An example of a single light ray (red line) interacting with a smoothed height-corrected synthetic magma ocean surface. Take note that the x-axis and y-axis do not have the same scale so the bouncing angle may seem distorted.

measurements. For each synthetic refractive index (n_{sy}) ranging from $1.5 - 6.0$ we generated multiple fractal terraines for Hurst exponents ranging from $0.95\,(\text{very smooth}) \rightarrow 0.01\,(\text{very rough})$. For each Hurst exponent value we simulated 10 morphologically different fractal surfaces where in each case we threw 10,000 light rays and recorded the average reflected component to estimate the planar albedo. However, planets are spherical so the planar albedo could not accurately describe their reflective properties (especially at high latitudes). Because of this, it is necessary to convert the planar albedo into the spherical albedo. By definition, the spherical albedo is the ratio of the monochromatic power reflected by a planet to the monochromatic power incident upon that planet, which is given as follows:

$$A_S = \frac{P_{refl}(\lambda)}{P_{in}(\lambda)} \tag{5a}$$

Where P_{refl} and P_{in} are the reflected and incident monochromatic powers respectively. The power incident upon the planet is given by:

$$P_{in} = F_{in}(\lambda) \cdot \pi R_p^2 \tag{5b}$$

Where $F_{in}(\lambda)$ is the monochromatic energy flux and R_p is the planetary radius. The power reflected by the planet is more complicated to calculate as one must determine how much light is reflected by each area segment of the planet,

as a function of the sub-stellar latitude (or longitude, as for tidally locked planets they are the same). The equation goes as follows:

$$P_{refl} = \int_0^{\pi/2} F_{in}(\lambda) \cos\phi \times q(\phi) \times 2\pi R_p^2 \sin\phi \; d\phi \tag{5c}$$

Where the first section is the monochromatic energy flux received from the star at a given sub-stellar latitude, the second part tells us how much light is reflected at a given sub-stellar latitude, and the third is the area at a given sub-stellar latitude. Although it may seem necessary to multiply Eq. 5c by two in order to account for the whole hemisphere ($\phi = -\pi/2 \rightarrow \pi/2$), one would also be required to multiply by a half to normalise the integral so that the total power arriving at the hemisphere is $F_{in}(\lambda) \cdot \pi R_p^2$, hence cancelling each other out. Nevertheless, we can now rearrange as follows:

$$P_{refl} = F_{in}(\lambda) \cdot \pi R_p^2 \int_0^{\pi/2} 2 \sin\phi \cos\phi \cdot q(\phi) \; d\phi \tag{5d}$$

Using the trigonometric identities,

$$P_{refl} = F_{in}(\lambda) \cdot \pi R_p^2 \int_0^{\pi/2} \sin 2\phi \cdot q(\phi) \; d\phi \tag{5e}$$

We can now divide Eq. 5e by 5b to get the spherical albedo:

$$A_S = \int_0^{\pi/2} \sin 2\phi \cdot q(\phi) \; d\phi \tag{6}$$

With the exception of idealised constructs like a Lambertian surface, $q(\phi)$ is never a constant. In order to determine $q(\phi)$, we ran another set of ray-tracing simulations for different refractive indices (n_{sy}), Hurst exponents (H), and sub-stellar latitudes (ϕ). The analytic approximation of $q(\phi)$, which incorporates the planar albedo, can be found in Sec.4. By solving Eq. 6 one can determine the spherical albedo, but before this is explored it is necessary to briefly discuss the possibility of atmospheric effects.

3.2. *Atmospheric Effects on the spherical albedo*

In this paper we focus on how the surface properties of a magma ocean effect the spherical albedo values of airless or near-airless, molten super-Earths. However, one could argue that the vaporised mineral atmospheres resulting from highly irradiated magmas could also affect the spherical albedo values. Fundamentally, this will depend on the composition of the magma and the resultant vaporised atmosphere. For volatile-free magmas, the secondary atmospheres would be thin due to the low refractory nature of rocky species (Schaefer and Fegley 2009; Ito et al. 2015). Furthermore, 1-D atmospheric models show that the high temperatures found on some of these hot super-Earths could prevent the formation of clouds within their daysides (Mahapatra et al. 2017). Therefore, one can consider the case of a thin, cloudless, mineral atmosphere on a hot molten super-Earth. Within this framework, two effects need to be considered. First, the Rayleigh scattering of gases should increase the planetary spherical albedo. Second, the spectroscopic absorption by the gases would decrease it.

The effects of Rayleigh scattering can be understood by considering Eq. 7:

$$\sigma_\lambda = \frac{128\pi^5}{3\lambda^4}\alpha^2, \tag{7}$$

where σ_λ is the Rayleigh scattering cross section for a given species, λ is the wavelength of light, and α is the static average electric dipole polarisability of the gaseous species being considered. According to the CRC Handbook (2011), the α values for the following species (in units of 10^{-24} cm^3) are: 24.11 for Na, 43.4 for K, 8.4 for Fe, 5.53 for Si, 10.6 or 11.1 for Mg, 0.802 for O, and 1.5689 for O_2 (for more information on these species, see CRC Handbook 2011, references therein). Due to having a large α and being one of the most abundant gases in mineral atmospheres, Na is expected to be the most scattering gas within these extreme environments (Schaefer and Fegley 2009; Ito et al. 2015). The effects of a pure Na mineral atmosphere is illustrated in Fig. 10 of Sec. F in the appendix where the optical depth from Rayleigh scattering is given for the case of Kepler-10b. It becomes clear how even for a strongly scattering mineral atmosphere, the influence on the spherical albedo becomes negligible for $\lambda \gtrsim 1$ μm.

Table 1. Parameters for Eq. (8a) and (8b)

Parameter	$H \leq 0.95$
α_1	-0.397910
α_2	0.149320
α_3	0.388928
α_4	0.852872
β_1	1.594982
β_2	-3.375571
β_3	2.437896
β_4	-0.881001
β_5	0.194354
β_6	-0.041750
β_7	-0.081323

Conversely, if the magma were to include several volatile elements such as H, C, N, S and Cl, then it would most probably be thick (Schaefer et al. 2012). In that case the scattering of the atmosphere would affect the spherical albedo value. However, the stability of highly volatile elements on close-in exoplanets against photoevaporation is still not well understood (Lopez 2017). For simplicity, in our paper we will only focus on the case where there is a volatile-free mineral atmosphere. However, we are aware that thick, cloud-free, atmospheres would have high albedo values in the optical range (Hamano et al. 2015).

Regarding Kepler-10b, whether the mineral atmosphere affects the albedo or not will depend on its composition, which we do not know with certainty. We give the case of sodium as it is the most optically thick of all non-volatile mineral atmospheric components (and hence, it is an interesting gas to consider). Sodium would affect the albedo at $\lambda = 0.5$ μm as its optical depth is $\simeq 1$. Nevertheless, our code is best adapted for larger wavelengths, primarily $\lambda > 1$ μm, so the effects of a mineral atmosphere should not be large. We are aware that the *Kepler* telescope operates at shorter wavelengths so one would expect the mineral atmosphere to contribute towards the spherical albedo. However, the high bolometric Bond albedo values inferred for Kepler-10b cannot fully be accounted for by a mineral atmosphere (Rouan et al. 2011), which is why we argue that an exotic magma must also be present.

We believe that in future works our code could be implemented into radiative transfer models where one could include clouds or a scattering atmosphere (see Sec. 5.6). Nonetheless, it is beyond the scope of our study to include atmospheric effects on the planetary spherical albedo as our paper focuses primarily on surfaces.

4. RESULTS

We were able to find an analytic relationship between the planar albedo (A_{pla}) of a molten surface and the Hurst exponent (H) as shown in Eq. (8a) and (8b). These equations were found by fitting the numerical data from our simulations. The raw data and its comparison to the planar albedo values predicted by Eq. (8a) and (8b) can be found in the Supplementary File 1. Within Supplementary File 1, we also show that the χ^2 values of our analytic approximation are small and hence we recommend its use over the raw data. For Hurst exponents greater than 0.95 the effects of roughness become negligible so Eq. 1b is an appropriate approximation for the planar albedo.

$$A_{pla} \approx (\alpha_1 H + \alpha_2) + (\alpha_3 H + \alpha_4)(1 - e^{\Psi \cdot n_{sy}}) \tag{8a}$$

with

$$\Psi = \beta_1 H^6 + \beta_2 H^5 + \beta_3 H^4 + \beta_4 H^3 + \beta_5 H^2 + \beta_6 H + \beta_7 \tag{8b}$$

Where $\alpha_{1\to4}$ and $\beta_{1\to7}$ are the coefficients listed in Table 1. Fig. 4 is a plot of Eq. (8a, 8b). Combining this result with the refractive indices from Polyanskiy (2010) and Grainger et al. (2014) gave us the planar albedo values for different materials at varying roughnesses and wavelengths. To convert the planar albedo into the spherical albedo, the dependence of the albedo on the sub-stellar latitude, $q(\phi)$, was required. From our simulations (see Supplementary File 2 for the raw data and χ^2 values) we found that $q(\phi)$ is well approximated as:

$$q(\phi) \approx 1 - \frac{1 - A_{pla}}{1 + \left(\frac{\phi}{\mathcal{C}_1(H)}\right)^{\mathcal{C}_2(H)}} \tag{9a}$$

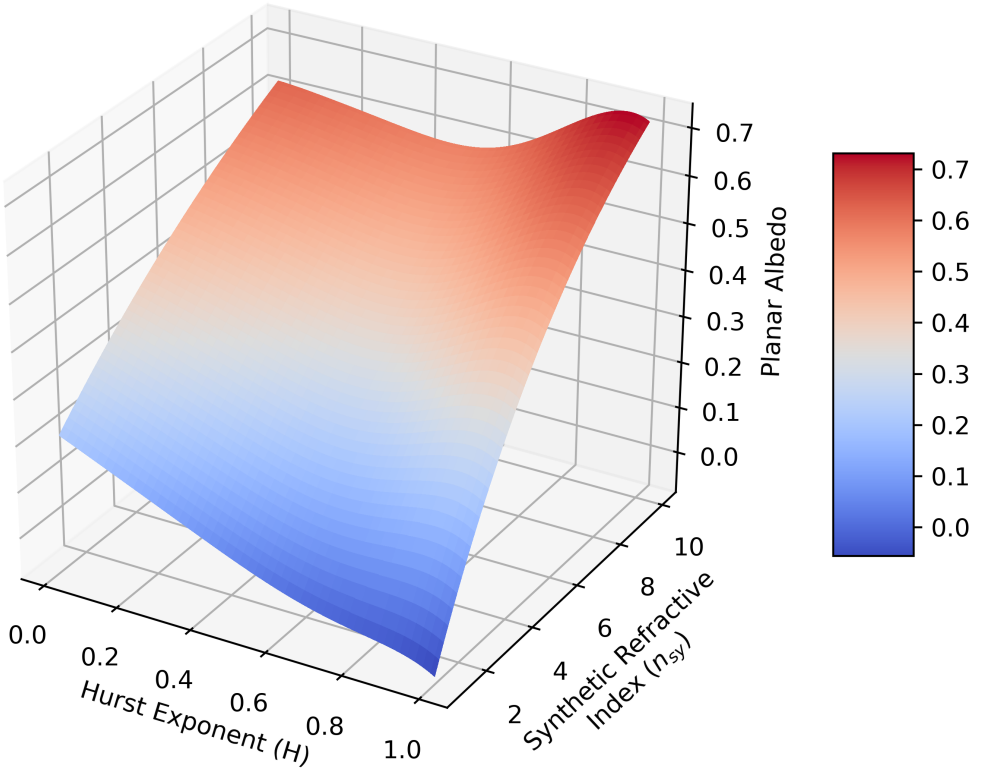

Figure 4. The planar albedo as a function of the synthetic refractive index (n_{sy}) and the Hurst exponent (H). This figure was generated with Eq. (8a) and (8b).

Where,

$$\begin{aligned} \mathcal{C}_1(H) &= 0.320717H + 1.14083 \\ \mathcal{C}_2(H) &= 8.54326 + 82.6376H^{3.88648} \end{aligned} \tag{9b}$$

From Eq. 9a it follows that as $\phi \to \pi/2$, $q(\phi) \to 1$ because at the terminator the planet is fully reflecting (at right angles there is no absorption). Conversely, when $\phi \to 0$, the local albedo becomes identical to the planar albedo as the light is interacting with the sub-stellar point. Combining Eq. 6 with Eq. 8a, (8b), (9a), and (9b) gives the spherical albedo of a planet. Hence, it is now possible to explore the reflective properties of planets with different magma ocean properties.

We begin by considering the spherical albedo of simple end-member magma compositions (see Fig. 9 in the appendix). We adopted a Hurst exponent of 0.8 which is consistent with the type of waves expected on Kepler-10b (see Sec. C in the appendix for more information). The best-fit equations for the numerical data of Polyanskiy (2010) and Grainger et al. (2014) are shown in Table 5 of Sec. E in the appendix. A brief summary of our results for the different materials is explained below (for a Hurst exponent of 0.8). The graphs showing the spherical albedo are shown in Sec. D of the appendix.

Planets composed of common Earth minerals and rocks typically have spherical albedo values of $\sim 10\%$. They also tend to drop as the wavelength increases from 0.5 μm to 7.8 μm. The only exceptions are SiO_2 (i.e. rhyolites) and komatiites which have sudden increases in their spherical albedos at ~ 7.2 μm.

Pure metal planets would have very high spherical albedos, especially if they were made of Ag, Al, Au, Cu, Fe, Mg, Mo, or Ni as they would reach values close to 100% at larger wavelengths. Metalloids (Ge and Si) would produce lower spherical albedos and within the wavelengths of interest, they appear to stabilise at $30 - 50\%$.

The reflective properties of metal oxides vary strongly depending on the species. FeO is the shiniest oxidised material analysed in this study with values reaching as high as 45%. Conversely, Al_2O_3 and MgO are the least reflective oxidised metallic species with spherical albedo values close to common Earth minerals and rocks such as the ones explained above.

We present two carbonaceous minerals; $CaCO_3$ and SiC. SiC's spherical albedo drops from $\sim 20\%$ to $\sim 15\%$ from $0.5 - 7.8$ μm respectively. Conversely, $CaCO_3$ has a spherical albedo $\lesssim 10\%$ for wavelengths below ~ 6.2 μm but beyond this it quickly increases to a maximum of almost $\sim 90\%$ at ~ 6.8 μm. This peak then drops to $\sim 15\%$ for wavelengths greater than ~ 7.5 μm.

Whilst Fig. (9) are useful for understanding the spherical albedo spectrum of pure materials; AMOPs are composed of multiple chemical species. It is therefore important to find geochemically self-consistent mixtures of the aforementioned materials so that from an observed albedo spectrum one can categorise the composition of an exoplanet. Hence, we propose the following categorisations for constraining exoplanet compositions from their spherical albedos: evolved molten bulk-silicate Earth (BSE) planets, metallic planets, coreless terrestrial planets (CTPs), reduced planets, and carbon-rich planets.

4.1. *Evolved Magmatic BSE Planet*

When a terrestrial planet with a BSE composition is subjected to temperatures above $\sim$ 1500 K, the minerals found within the magma begin to vaporise (e.g. Schaefer and Fegley 2009; Schaefer et al. 2012; Ito et al. 2015). This vaporisation could lead to a strong evolution in the chemical composition of the magma (Kite et al. 2016). It therefore follows that the physical and optical properties of the lava should also change with time. In Fig. 5 we show our predicted spherical albedo spectrums for a BSE airless planet under 4 different levels of vaporisation: 0%, $\lesssim$ 80%, $\sim$ 92%, and $\sim$ 100%. The first has a typical BSE composition (O'Neill and Palme 1998) whilst the latter three approximately correspond to 60 : 40 of $MgO - SiO_2$, 50 : 50 of $CaO - Al_2O_3$, and pure Al_2O_3 respectively.

Our synthetic spectrums predict spherical albedos lower than $\sim 11\%$. Due to current limitations in our astronomical instrumentation there appears to be no clear way of distinguishing between different types of Earth-like compositions regardless of how evolved the magma is. Notwithstanding, our findings suggest than a spherical albedo value of $\sim 11\%$ or lower, with a decrease at longer wavelengths, is suggestive of a composition similar to the Earth's.

4.2. *Metallic Planet*

Prior to considering the spherical albedo values of metallic planets it is important to understand their formations. One can begin by analysing Mercury that has an estimated bulk iron abundance of $\sim 70\%$ (e.g. Riner et al. 2008; Malavergne et al. 2010; Hauck et al. 2013; Chabot et al. 2014). There are three main explanations for this super-ferruginous composition: thermally-induced surface vaporisation (e.g. Cameron 1985), collisional stripping (e.g. Benz et al. 1988), and chemical/thermal gradients within the primordial solar nebula triggering an unusual formation (e.g. Lewis 1972, 1974). For larger bodies such as super-Earths, surface vaporisation would be unable to trigger sufficient mass-losses as the required escape velocities of silicate species are too large (Ito et al. in prep). Regarding collisional stripping, Marcus et al. (2010) showed that the maximum amount of iron that a super-Earth could have is $\sim 70\%$ which is compatible with the abundance in Mercury. Finally, forming iron-rich exoplanets due to chemical/thermal gradients has been shown to be possible in our solar system (e.g. Lewis 1972, 1974), and considering how iron is the sixth most abundant element in the universe (by mass) there does not appear to be a strong argument against this mechanism either. We are therefore left with the latter two mechanisms for the formation of metal-rich super-Earths.

Before one can explore the outcomes that could arise from these two dissimilar formation mechanisms, it is necessary to issue the following caveat: a bulk iron composition is not implicative of a surface also containing iron. For example, Mercury's surface composition is very iron-poor $1 - 2$ wt.% (Evans et al. 2012; Weider et al. 2014) which may seem paradoxical at first. There is a straightforward explanation for this; Mercury formed from very reduced materials. We will discuss reduced planets more in-depth in section 4.4. Notwithstanding, if a terrestrial exoplanet were to form under very oxidised conditions, a large portion of its total iron would bind with oxygen to form the usual oxides (FeO, Fe_2O_3, and Fe_3O_4). These compounds are less dense than pure metals or alloys so they would become incorporated into rock-forming minerals such as olivine and pyroxenes that would then form the mantle and crust (Elkins-Tanton and Seager 2008). Conversely, the pure iron and iron-nickel alloys would sink to the centre of the planet thus forming a core. Following this line of thought, after a certain critical level of oxygen, all of the iron would form oxides therefore leaving the planet coreless (see Sec. 4.3). It is therefore very important not to assume that an iron-rich world will

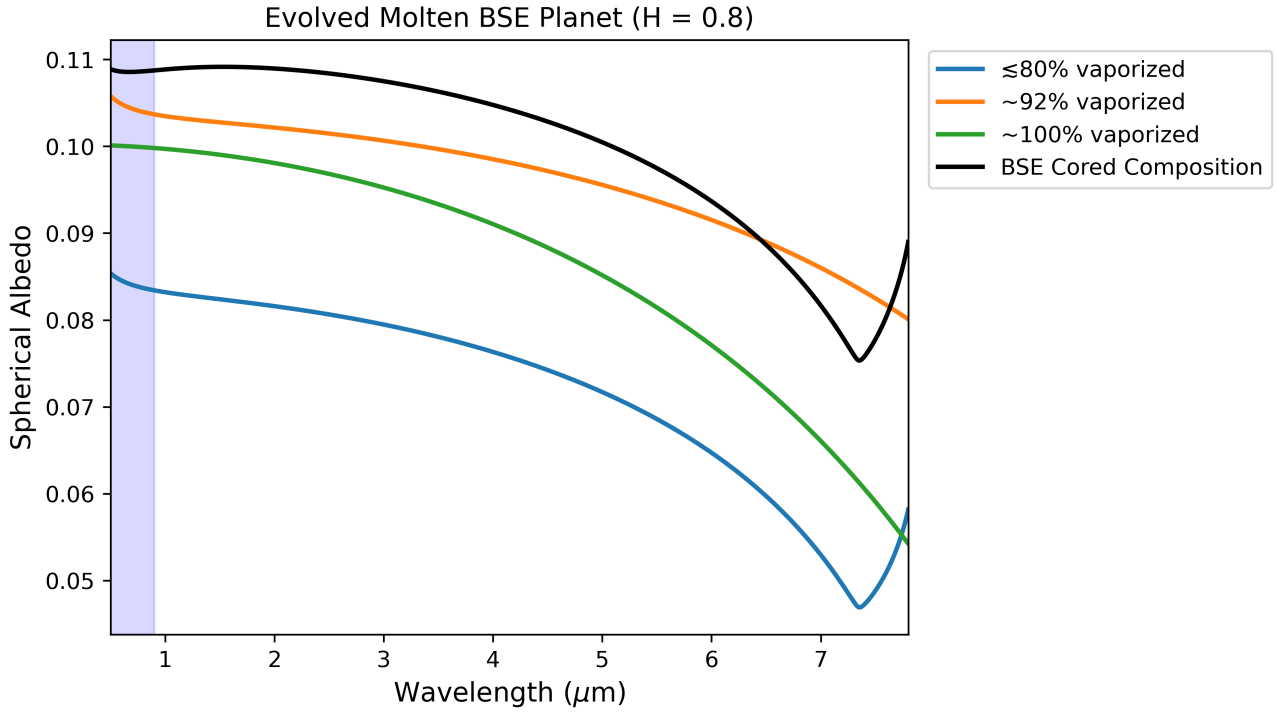

Figure 5. The spherical albedo for a terrestrial planet with an initial composition corresponding to the BSE that has been evolved due to chemical interactions between the magma and the mineral atmosphere. Four different spherical albedo spectrums are shown corresponding to varying levels of vaporisation. The BSE composition is from O'Neill and Palme (1998) whilst the vaporised compositions were taken from Kite et al. (2016). The light-blue section is *Kepler's* band-pass. This figure was generated with Eq. (6), (8a), (8b), (9a), and (9b).

host an iron-rich surface as the stability of metals in the crust and mantle are strongly dependent on the presence of oxygen. Keeping in mind the above caveat, one can now refer back to the two distinct formation mechanisms and show how they can lead to two geochemically distinct magmas.

According to the collisional-stripping model, a planet becomes Fe-rich *after* its formation due to the partial removal of the mantle, while its core remains relatively intact. Therefore, the abundance of iron in the mantle and crust (from which the magmas are formed) is approximately independent of any collisions (excluding exogenous deposits). It then follows that the Fe-richness of metallic exoplanets' magmas is more strongly dependent on the presence of oxygen than the bulk abundance of iron. Conversely, if iron planets form due to thermal/chemical gradients in the primordial stellar nebula then there could be a relationship between being oxygen-poor and iron-rich. This is best explained by briefly summarising the requisites for both of these outcomes:

- At very high temperatures $MgSiO_3$ is weakly captured whilst iron condenses with relative ease (e.g. Lewis 1972, 1974). Consequently, under these conditions the minerals that form are richer in iron-bearing minerals and poorer in silicates than elsewhere in the stellar nebula.

- At very high temperatures the chondrules that form enstatite chondrites are created from supercooled, fluid, silicate, rain-like droplets (Blander et al. 2009). These reduced chondrites are believed to be the materials that form reduced planets such as Mercury (e.g. Nittler et al. 2011; Malavergne et al. 2014; Nittler and Weider 2019).

In contrast to the collisional stripping model, if iron-planets form from chemical/thermal gradients, having a high abundance of iron might coincide with being reduced. This would result in most of the iron being captured within the core and little being left within the mantle. Therefore, according to this mechanism, metallic exoplanets could have felsic magmas that are sulfur-rich (e.g. Haughton et al. 1974; McCoy et al. 1999; Namur et al. 2016).

Table 2. Predicted Bulk Chemical Composition of Coreless Terrestrial Planets (CTPs)

Chemical	Abundance (%)
O	35.2
Si	13.5
Fe	37.8
Mg	11.3
Ca	1.1
Al	1.1

NOTE—Based on the findings from Elkins-Tanton and Seager (2008)

To summarise, the magma composition of metallic planets is strongly dependent on the formation mechanisms and history of the planet. Hence, we believe that the bulk iron mass-fraction cannot be constrained from the measured spherical albedo spectrum of these types of bodies.

4.3. *Coreless terrestrial Planet*

In order to model coreless terrestrial planets (CTPs) we first had to set a planetary bulk composition and then subject it to the relevant thermodynamic conditions. In order to do so we used the elemental composition listed in Table 2 with the temperature and pressure shown in Table 4 (see appendix) and then applied the GGCHEM geochemical code (Woitke et al. 2018). Our resultant magma composition is well approximated as 60 : 40 of iron oxides to enstatite which is much more iron-rich than the BSE ($\lesssim 10\%$ iron oxides). However, because GGCHEM simulates only FeO as the Fe-bearing oxide in liquid phases, it does not specify the ratio of FeO : Fe_2O_3 : Fe_3O_4. As shown in Fig. 9, the spherical albedo values of these species differ moderately so one cannot treat all of them as FeO. We will therefore present the upper- and lower-bounds with the average spherical albedo for a given Hurst exponent (Fig. 6).

Our results show that coreless bodies have much higher spherical albedos than their differentiated counterparts with similar compositions. This is due to iron-oxides being shinier (see Fig. 9) and more abundant in CTP magmas. The uncertainty in the spherical albedo is due to the different possible ratios of FeO : Fe_2O_3 : Fe_3O_4, which is dependent not only on the Gibbs energies but also on how much oxygen was present during the formation of the body. Whilst one might not be able to differentiate between which iron oxides are present within the magma, one could make a strong argument for the presence of iron within these bodies. Adjusting the surface roughness parameter (H) and maximising the FeO abundance allows for a theoretically maximum spherical albedo of $\sim 55\%$.

4.4. *Reduced Planet*

In order to understand the formation mechanism of reduced planets, one can analyse Mercury which is the most reduced planet in our solar system (e.g. Nittler et al. 2011; Malavergne et al. 2014; Nittler and Weider 2019). This is probably because it formed from enstatite chondrites which are extremely reduced (Blander et al. 2009). These rocks can be classified into two groups; EH (high enstatite) and EL (low enstatite) chondrites. Each group has slightly different chemical makeups (Wasson and Kallemeyn 1988) but their close similarities allow for an approximate average composition to be deduced (see Table 3, Javoy et al. 2010).

By applying the GGCHEM code (Woitke et al. 2018) with the elements listed in Table 3, the temperature and pressure shown in Table 4, we predict a magma composed of over $\gtrsim 90\%$ pure Fe with the rest mostly comprising typical terrestrial silicate minerals such as forsterite and spinel. The reason why the Fe concentration in the magma is much higher than the one shown in Table 3 is because one also has to consider the composition of the emitted gas. This vaporised atmosphere contains many of the volatile elements that used to be present in the melt. Nevetheless, because of gravity, the pure iron would sink to the planet's core thus resulting in an iron-poor mantle. These predictions are strongly corroborated by observational (e.g. Evans et al. 2012; Weider et al. 2014) and geophysical (e.g. Riner et al. 2008; Hauck et al. 2013) data of Mercury. Furthermore, spinel, fosterite and many of the other silicate minerals that are predicted by the GGCHEM geochemical code are the same materials that makeup large portions of Earth's mantle. These silicates would be molten within the high temperature ranges we are focusing on in this paper. In other words, from a reduced planet made of enstatite chondrites (or from similarly reduced rocks) we would expect silicate-rich magmas that are iron-poor. A rhyolitic magma could be a good contender due to being very SiO_2-rich (typically $\gtrsim 69\%$; Le Maitre et al. 2002). If rhyolites were to be the most common magmas on reduced super-Earths then from

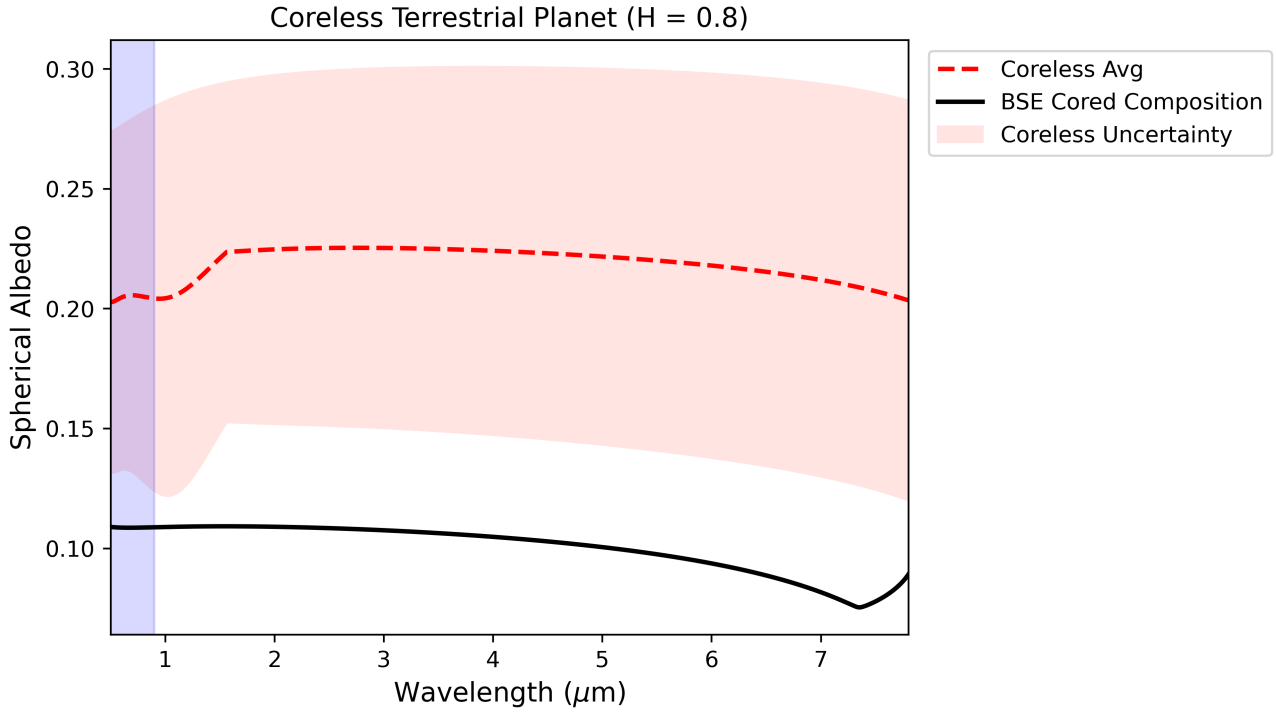

Figure 6. The spherical albedo of a coreless terrestrial planet with the composition given by Elkins-Tanton and Seager (2008). The red dotted line is the average coreless spherical albedo value for $H = 0.8$, the red shaded region represents the uncertainty, and the black line is for the spherical albedo value of a cored BSE planet (O'Neill and Palme 1998). The light-blue section is *Kepler's* band-pass. This figure was generated with Eq. (6), (8a), (8b), (9a), and (9b).

Table 3. Predicted Bulk Chemical Composition of Reduced Planets

Chemical	Abundance (%)
O	33.3
Si	20.2
Fe	28.3
Mg	14.0
Ca	1.0
Al	0.97
Ni	1.73
Ti	0.06
Cr	0.36
Co	0.08

NOTE—Based on the findings from Javoy et al. (2010)

Fig. 9 it can be seen that spherical albedo values less than 10% would be expected. However, other exotic magmas that are oxygen-poor could also be possible. For instance, if a planet were carbon-rich then carbonaceous magmas might exist. We discuss this concept in Sec. 4.5.

Finally, we would like to briefly discuss one potential way of forming a reduced, airless, molten planet with pure iron deposits on its surface. Suppose a planet were to form under very cold conditions, this would result in most of the oxygen bonding with silicon, carbon, hydrogen and magnesium. Considering how iron is not a very aerophilic element, some of it may be left in its elemental form. If this planet were then to migrate very close to its host

star, XUV-irradiation may fully erode away its atmosphere leaving behind a denuded core (e.g. Lecavelier Des Etangs 2007; Ehrenreich and Désert 2011; Lammer et al. 2013; Owen and Wu 2013; Jin et al. 2014; Owen and Wu 2017; Jin and Mordasini 2018; Kubyshkina et al. 2018; Locci et al. 2019; Modirrousta-Galian et al. 2020a). Due to iron being relatively heavy, it may be resilient to hydrodynamic escape (e.g. Zahnle and Kasting 1986; Hunten et al. 1987; Luger and Barnes 2015) which could result in pure iron deposits being left behind on the bare core. Pure iron is very reflective (see Fig. 9) so it is possible for these planets to have very high spherical albedo values if there were to be a copious abundance of iron in its elemental form. Undeniably, the stability of pure iron within a lava matrix would be subjected to the usual caveats of the circulation and sinking timescales. These systems are highly speculative and warrant more research.

In summary, the spherical albedos of reduced planets that form from enstatite chondrites should be very low ($\lesssim 10\%$) as their surfaces are expected to be rich in silicate species. We find that the amount of light they reflect is similar to that of BSE composition planets, albeit with slighly different spectrum shapes. However, one cannot rule out the possibility of more unusual formation mechanisms which could lead to an ambiguity in the predicted spherical albedos.

4.5. *Carbon-rich Planet*

There are several arguments for carbon-rich super-Earths such as the existence of carbonaceous bodies in our solar system (e.g. c-type asteroids) and the presence of main sequence stars with high carbon-to-oxygen ratios (C/O). These stars could host these exotic worlds, especially since theoretical modelling predicts that even with moderate C/O ratios several carbon-rich worlds could form (Moriarty et al. 2014). However, as of February 2020 there are no known carbon-rich super-Earths. Because of this limitation we will base our magma composition on theoretical principles. We will avoid using pure carbon (Madhusudhan et al. 2012) as the minimum melting points of carbon allotropes tend to be > 4000 K (e.g. Bundy 1989; Bundy et al. 1996; Correa et al. 2006), which is generally beyond the equilibrium temperature of most super-Earths. Hence, we will adopt a more chemically diverse composition such as the one delineated in Miozzi et al. (2018).

Whilst SiC has been found in presolar grains (e.g. Lodders and Fegley 1995; Hoppe et al. 2010), it has a tendency to decompose due to the high affinity between oxygen and silicon. For instance, if a planet were to be composed of equal parts Si-O-C, most of the silicon would bind with the oxygen to form silicates such as SiO_2 and SiO. The carbon would then bond with itself to form graphite in the outer layers of the planet and diamond at greater depths. Due to graphite being less dense than SiO_2 and having a higher melting temperature, it would rise to the top layers of the mantle in the form of solid graphitic grains. Our simple analogy is strongly supported by high-pressure, high-temperature (high P-T) laboratory experiments (e.g. Hakim et al. 2018, 2019) that arrived at the same conclusion, albeit in more detail. These high P-T experiments predict that extremely reduced conditions would be required in order to maintain SiC in a geochemically stable condition. Therefore, in spite of SiC planets being theoretically plausible, they may be unlikely. Notwithstanding, we included the spherical albedo of SiC in Fig. 9.

On that account, it seems more probable that carbon-rich worlds will be composed of silicate mantles covered in solid graphite. The spherical albedo values of these planets would therefore be dominated by the graphitic layer which we cannot model with our code due to it being adapted for fluid systems. If one ignores surface roughness, the spherical albedo of a graphite layer within the range of $0.5 - 7.8$ μm would vary from $30 - 80\%$ (e.g. Taft and Philipp 1965; Philipp 1977; Querry 1985; Djurišić and Li 1999; Kuzmenko et al. 2008; Papoular and Papoular 2014), which would make carbon-rich super-Earths the brightest airless bodies listed in our paper.

5. DISCUSSION

Measuring, constraining, and interpreting the spherical albedo of exoplanets is an active area of research which is mostly limited by observational constraints. With the JWST expected to launch in 2021, the *Atmospheric Remote-sensing Infrared Exoplanet Large-survey* (ARIEL) in 2028, a more in-depth analysis could be possible. Because of this we now provide two tests that could be used to constrain the magma composition of molten super-Earths from their spherical albedo values:

5.1. *Optimistic Test: High Precision High Accuracy Measurements (HPHA)*

In the ideal case scenario, the extracted albedo spectra from the aforementioned missions would be robust enough to perform statistical tests on them (e.g. MCMC algorithms). The shape of the spectrum would be the major source of information for the surface composition whilst the amplitude would mostly determine the surface roughness (i.e.

the Hurst exponent). The experimental data that relates a material's refractive index to the wavelength of light began almost a century ago and it is ongoing. From these relationships, Eq. (1c), (6), (8a), (8b), (9a), and (9b) could be used to constrain the surface compositions of molten, airless super-Earths. Because of this, regardless of whether ARIEL or the JWST missions could extract HPHA measurements, it is certainly possible that in the future the spherical albedo spectrum of a planet could be matched to a certain composition in a similar fashion to how exoplanet atmospheres are being constrained from spectroscopic data.

5.2. *Conservative Test: Low Precision Low Accuracy Measurements (LPLA)*

A more realistic scenario is that a few albedo measurements at varying wavelengths with considerable uncertainties are extracted. For this scenario we propose a test that will most probably be possible for ARIEL and the JWST missions once an optically thick atmosphere is excluded (i.e. the planet is airless or near-airless). We propose that based on the mass and radius of an observed AMOP one limits the possible internal compositions. From this information, the observed albedo spectrum is compared to our five compositional categories described in sections 4.1, 4.2, 4.3, 4.4, and 4.5. For instance, in the case of Kepler-10b the mass and radius measurements are consistent with a coreless or near-coreless interior which is illustrated in Fig. 1. Therefore, whilst the spherical albedo is very uncertain, an extremely ultramafic magma is compatible with the values shown in Fig. 6.

5.3. *The Effects of Changing the Hurst Exponent (H)*

In Fig. 4 we show how the Hurst exponent and the synthetic refractive index affect the planar albedo of a system. However, understanding the isolated influence that the H parameter has may be difficult to picture so we have included Fig. 7. Although the shape of the spectrum is slightly affected by varying H, the most prominent change is in the amplitude. This is an important point to consider as it implies that strong deviations in the shape of the retrieved albedo spectrum are most probably due to compositional differences between the adopted (predicted) magmas and the ones that are observed. From an observational perspective, this lowers the degeneracy of the inferred surface properties from the observed spherical albedo as the effects from the surface roughness (H) and the composition can be partially isolated.

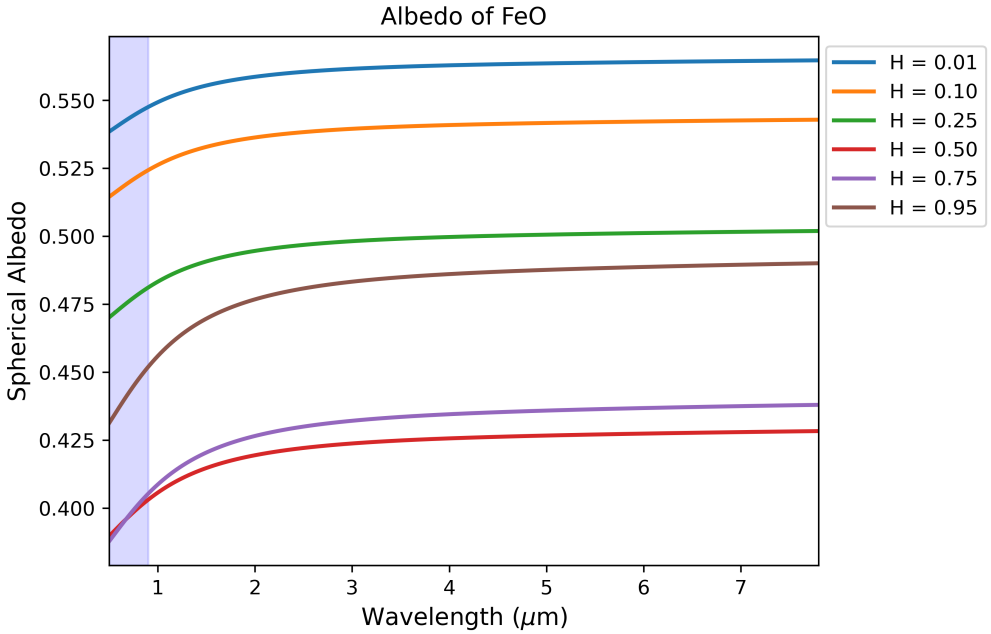

Figure 7. The spherical albedo of FeO for different Hurst exponents and wavelengths. The light-blue section is *Kepler's* band-pass. This figure was generated with Eq. (6), (8a), (8b), (9a), and (9b).

5.4. *Comparing our Results with Hu et al. (2012)*

Our study focuses on molten airless bodies whilst Hu et al. (2012) focuses on solid ($T_{eff} = 300 - 880$ K) planetary surfaces so there will be inevitable differences in our results. For instance, for solid systems the surface roughness is affected by grain configurations and sizes (e.g. Bennett and Porteus 1961), which is very hard to model mathematically. In their study, fine grained surfaces were assumed when constructing their synthetic spectra. This will lead to an overestimation of the albedo value as finer grains typically have higher albedos than their coarser-grained counterparts. Because of this they point out that their results are "upper limits". This is further emphasised in our study, as in Fig. 7 we show that differences in the surface roughness could change the spherical albedo values by $\sim 15\%$ for certain materials. However, this alone might not fully explain the different albedo values calculated by our study and theirs, so below we will explore other possibly reasons:

- **Basaltic:** Their basaltic values are much higher than our results as well as Pollack et al. (1973), Egan et al. (1975), Shestopalov et al. (2013), and Fornasier et al. (2016). One possibility is that they used very young basaltic powder which can be several times more reflective than older specimens. The reason why there is a darkening with age is due to interactions between the basalt grains and the H-ions from solar winds (Shestopalov et al. 2013; Fornasier et al. 2016).

- **Fe-oxydised**: In their paper, they adopt a composition of 50% Fe_2O_3 (haematite) and 50% basalt, with which they predict an albedo of $10 - 20\%$. This is consistent with our results as we predict a basaltic albedo of $2 - 7\%$ and a value of $20 - 30\%$ for Fe_2O_3, so a $50:50$ mixture could reproduce their results.

- **Metal-rich:** We consider planets that are rich in metals (bulk), which as explained in Sec. 4.2 would result in metal-poor surfaces. Conversely, in Hu et al. (2012) they adopt an FeS_2 composition.

- **Ultramafic:** Their ultramafic albedo is large, but it could be explained by a very high concentration of metal oxides (see Sec. 4.3). However, if we assume that Hu et al. (2012) used a moderate metal oxide abundance then their results would be substantially larger than ours (see Fig. 6). This may be explained by their fine-grained assumption and the possibility that they used very young basaltic specimens.

Whilst the results from Hu et al. (2012) differ moderately from ours, we are working in two different regimes: molten versus solid. Thus, we do not feel like there is a contradiction between our spherical albedo values and theirs. However, we are aware that our model has its own limitations that could be improved upon in the future. We list these limitations in Sec. 5.5.

5.5. *Limitations of our Model*

Our model has limitations that need to be noted by anyone who wishes to use it. Here we present a list of shortcomings and how they could be improved upon by future research:

- *We used Earth's oceans as an analogue for the roughness of the magma oceans of airless or near-airless molten planets.* We used this approximation twice: when applying the Gaussian filter to the pre-smoothed synthetic magma ocean surfaces (i.e. Fig. 2), and when solving for the constant h_0 in Eq. 3. The question one might ask is whether the viscosity of lava is comparable to that of water in order for surface perturbations (such as waves) to be similar. Using the Vogel–Fulcher–Tammann equation (Vogel 1921; Fulcher 1925a,b; Tammann and Hesse 1926) the similar dynamical viscosities of these two fluids can be shown:

$$\log_{10}(\mu) = A + \frac{B}{T - C} \tag{10}$$

  Where μ is the dynamic viscosity at T which is the temperature of interest; A, B, and C are experimentally-determined constants, which depend on the composition of the magma. If one were to set the temperature high enough one can see how the viscosity drops precipitously. Let T be the day-side temperature of Kepler-10b ≈ 2750 K and for the experimental constants we will adopt the values for peridotite (Dingwell et al. 2004): $A \simeq -4.31$, $B \simeq 3703$, $C \simeq 761.7$. These values give $\mu \approx 10^{-2.5}$ Pa s which is only twice as viscous as water (Viswanath and Natarajan 1989). This result is compatible with other studies which are consistent with water-like lava viscosities at very high temperatures (e.g. Russell et al. 2004; Giordano et al. 2008). A similar

calculation can be done for metals to show that at high temperatures they have very low viscosities (e.g. de Wijs et al. 1998).

It is important to note that our model will only work for fluid surfaces. For example, for silicate planets effective temperatures $\gtrsim 1500$ K will result in magma oceans. Moreover, higher temperatures will increase the accuracy of our model as the melt viscosities will approach that of water. For other materials the conditions will differ, such as a carbonatite magma that at $\simeq 800$ K will be molten and have a viscosity similar to that of water. Nevertheless, we are aware that the viscosity of the magma oceans depends on many parameters such as the composition, the spherical albedo, and the effective temperature of the planet. These are important parameters that should be investigated further but they are beyond the aims of our study.

- *We assumed that the refractive index is independent of the temperature of the system.* We are aware that this is a strong simplification as, for example, Ge and Si's refractive indices grow by approximately $\sim 5\%$ as their temperatures increase from 100 K to 600 K (Li 1980). We also lack experimental data on how the refractive indices evolve when there is a phase change which could be problematic as we use the refractive indices for the solid phases whilst magmas are fluids. However, as shown by Essack et al. (2020), the albedo of 100% molten and 100% solidified basaltic glass remains relatively constant which implies that the refractive indices might not vary too strongly. In any case, the dependence of the refractive indices on the temperature and phase of the materials are poorly constrained and warrant more research. This limitation can be fixed with relative ease; whenever a better data set is discovered for a given material one can replace the n and k or n_{sy} values given in table 5 with the improved ones. This new data could then be used within Eq. (6), (8a), (8b), (9a), and (9b).

- *We did not account for the albedo contribution from small, solid, undissolved particles i.e. single-scattering albedo.* The presence of solid undissolved particles could strongly influence the spherical albedo of a planet. As explained by Rouan et al. (2011), molecules such as UO_2 and ThO_2 would not dissolve in certain melts such as an $Al_2O_3 - CaO$ matrix and they would be solid. Other molecules such as MgO and CaO also have very high fusion temperatures but they are more commonly dissolved. Notwithstanding, spherical albedos as high as $\sim 50\%$ may be caused by such minerals, so planets like Kepler-10b may be very reflective because of their presence. Our model does not account for these particles but one could separately include their contribution therefore overcoming this limitation.

- *We assume that the spherical albedo becomes independent of the Hurst exponent for* $H > 0.95$. In reality the spherical albedo would change for surface roughnesses ranging from 0.95 to 1.0. However, it becomes exceedingly difficult to model such surfaces as the ocean stops behaving fully like a fractal and starts having properties more akin to simple geometrical shapes. Because of this, the Davies-Harte (Davies and Harte 1987) method cannot be used. Hence, considering how the spherical albedo values of surfaces with Hurst exponents of 0.95 are very close to that of $H = 1.0$; we approximated the surfaces as being flat for $0.95 < H < 1.0$ (i.e. Eq. 1b).

5.6. *Future Work*

There is a bimodal distribution of exoplanet radii with one peak at $\sim 1.3 R_\oplus$, the other at $\sim 1.75 R_\oplus$, and the minimum at $\sim 2.4 R_\oplus$ (Fulton et al. 2017). According to theoretical modelling (e.g. Owen and Wu 2013, 2017; Jin and Mordasini 2018; Modirrousta-Galian et al. 2020a) and observational data (e.g. Swain et al. 2019) most planets in the first peak are lacking a hydrogen atmosphere whilst most planets in the second peak have large hydrogen envelopes. On the one hand, for planets with hydrogen atmospheres it is much easier to constrain their compositions as atmospheric species can be detected (Tsiaras et al. 2016; Ridden-Harper et al. 2016; Esteves et al. 2017) and then used to infer some interior properties. On the other hand, if a planet lacks a large hydrogen component then spectroscopy may not be feasible which leaves one with less data to deduce interior properties. In the case of molten, airless super-Earths (located mostly within the first peak) the spherical albedo could be used in an analogous manner to spectroscopic data in order to deduce the surface composition and hence constrain the interior structure. Hence, one could test exotic bodies like 55 Cancri e which could either be a coreless body (Bourrier et al. 2018), a carbonaceous planet (Madhusudhan et al. 2012; Miozzi et al. 2018), an icy planet (Zeng and Sasselov 2013; Zeng et al. 2016), or a planet with a hydrogen atmosphere partially confined to the nightside and with a dayside that is near-airless (Modirrousta-Galian et al. 2020b).

In addition, due to our code being analytic, it could be implemented into atmospheric general circulation models (GCMs) or spectral retrieval codes. This might provide a more holistic analysis of a planet since the effects of an

atmosphere and those of the surface could be better coupled. Furthermore, it would be interesting to expand our work to non-molten surfaces such as desert planets. In theory, solid surfaces could also be explained using fractal mathematics (e.g. Mandelbrot 1975; Shelberg et al. 1983). We would also welcome more experimental data on the refractive indices of materials at different temperatures, pressures, and phases in order to better model the spherical albedo values of exoplanetary surfaces.

6. CONCLUSIONS

In this paper we present an analytic model for the spherical albedo of molten, airless or near-airless super-Earths. We developed this model by fitting the results from the simulations of photons interacting with magma ocean surfaces that had varying reliefs and geochemical compositions. Our list shown in Table 5 is not comprehensive as there are many potential chemicals that could be added to the collection. Due to being analytic in nature, our model could be adopted in a computationally inexpensive manner in order to constrain the surface composition of some exoplanets.

ACKNOWLEDGEMENTS

We acknowledge the support of the ARIEL ASI-INAF agreement n. 2018-22-HH.0. We also thank the researchers and staff at the Telescopio Nazionale Galileo, La Palma (Spain) for introducing us to Kepler-10b that inspired us to carry out this study. We are grateful to Podolak M. and the anonymous referees for their useful comments.

REFERENCES

M. Abraham and R. Becker. *The Classical Theory of Electricity and Magnetism*. Blackie and Son, 2 edition, 1950.

T. Amotchkina, M. Trubetskov, D. Hahner, and V. Pervak. Characterization of e-beam evaporated Ge, YbF3, ZnS, and LaF3 thin films for laser-oriented coatings. *ApOpt*, 59(5):A40, Feb 2020. https://doi.org/10.1364/AO.59.000A40.

Astropy Collaboration, T. P. Robitaille, E. J. Tollerud, P. Greenfield, M. Droettboom, E. Bray, T. Aldcroft, M. Davis, A. Ginsburg, A. M. Price-Whelan, W. E. Kerzendorf, A. Conley, N. Crighton, K. Barbary, D. Muna, H. Ferguson, F. Grollier, M. M. Parikh, P. H. Nair, H. M. Unther, C. Deil, J. Woillez, S. Conseil, R. Kramer, J. E. H. Turner, L. Singer, R. Fox, B. A. Weaver, V. Zabalza, Z. I. Edwards, K. Azalee Bostroem, D. J. Burke, A. R. Casey, S. M. Crawford, N. Dencheva, J. Ely, T. Jenness, K. Labrie, P. L. Lim, F. Pierfederici, A. Pontzen, A. Ptak, B. Refsdal, M. Servillat, and O. Streicher. Astropy: A community Python package for astronomy. *A&A*, 558:A33, Oct. 2013. https://doi.org/10.1051/0004-6361/201322068.

Astropy Collaboration, A. M. Price-Whelan, B. M. Sipőcz, H. M. Günther, P. L. Lim, S. M. Crawford, S. Conseil, D. L. Shupe, M. W. Craig, N. Dencheva, A. Ginsburg, J. T. VanderPlas, L. D. Bradley, D. Pérez-Suárez, M. de Val-Borro, T. L. Aldcroft, K. L. Cruz, T. P. Robitaille, E. J. Tollerud, C. Ardelean, T. Babej, Y. P. Bach, M. Bachetti, A. V. Bakanov, S. P. Bamford, G. Barentsen, P. Barmby, A. Baumbach, K. L. Berry, F. Biscani, M. Boquien, K. A. Bostroem, L. G. Bouma, G. B. Brammer, E. M. Bray, H. Breytenbach, H. Buddelmeijer, D. J. Burke, G. Calderone, J. L. Cano Rodríguez, M. Cara, J. V. M. Cardoso, S. Cheedella, Y. Copin, L. Corrales, D. Crichton, D. D'Avella, C. Deil, É. Depagne, J. P. Dietrich, A. Donath, M. Droettboom, N. Earl, T. Erben, S. Fabbro, L. A. Ferreira, T. Finethy, R. T. Fox, L. H. Garrison, S. L. J. Gibbons, D. A. Goldstein, R. Gommers, J. P. Greco, P. Greenfield, A. M. Groener, F. Grollier, A. Hagen, P. Hirst, D. Homeier, A. J. Horton, G. Hosseinzadeh, L. Hu, J. S. Hunkeler, Ž. Ivezić, A. Jain, T. Jenness, G. Kanarek, S. Kendrew, N. S. Kern, W. E. Kerzendorf, A. Khvalko, J. King, D. Kirkby, A. M. Kulkarni, A. Kumar, A. Lee, D. Lenz, S. P. Littlefair, Z. Ma, D. M. Macleod, M. Mastropietro, C. McCully, S. Montagnac, B. M. Morris, M. Mueller, S. J. Mumford, D. Muna, N. A. Murphy, S. Nelson, G. H. Nguyen, J. P. Ninan, M. Nöthe, S. Ogaz, S. Oh, J. K. Parejko, N. Parley, S. Pascual, R. Patil, A. A. Patil, A. L. Plunkett, J. X. Prochaska, T. Rastogi, V. Reddy Janga, J. Sabater, P. Sakurikar, M. Seifert, L. E. Sherbert, H. Sherwood-Taylor, A. Y. Shih, J. Sick, M. T. Silbiger, S. Singanamalla, L. P. Singer, P. H. Sladen, K. A. Sooley, S. Sornarajah, O. Streicher, P. Teuben, S. W. Thomas, G. R. Tremblay, J. E. H. Turner, V. Terrón, M. H. van Kerkwijk, A. de la Vega, L. L. Watkins, B. A. Weaver, J. B. Whitmore, J. Woillez, V. Zabalza, and Astropy Contributors. The Astropy Project: Building an Open-science Project and Status of

S. Babar and J. H. Weaver. Optical constants of Cu, Ag, and Au revisited. *ApOpt*, 54(3):477, Jan 2015. https://doi.org/10.1364/AO.54.000477.

N. M. Batalha, W. J. Borucki, S. T. Bryson, L. A. Buchhave, D. A. Caldwell, J. Christensen-Dalsgaard, D. Ciardi, E. W. Dunham, F. Fressin, and I. Gautier, Thomas N. Kepler's First Rocky Planet: Kepler-10b. *ApJ*, 729(1):27, Mar 2011. https://doi.org/10.1088/0004-637X/729/1/27.

H. E. Bennett and J. O. Porteus. Relation between surface roughness and specular reflectance at normal incidence. *J. Opt. Soc. Am.*, 51(2):123–129, Feb 1961. https://doi.org/10.1364/JOSA.51.000123. URL http://www.osapublishing.org/abstract.cfm?URI=josa-51-2-123.

W. Benz, W. L. Slattery, and A. G. W. Cameron. Collisional stripping of Mercury's mantle. *Icarus*, 74(3): 516–528, Jun 1988. https://doi.org/10.1016/0019-1035(88)90118-2.

M. Blander, A. D. Pelton, and I. H. Jung. A condensation model for the formation of chondrules in enstatite chondrites. *Meteoritics and Planetary Science*, 44(4): 531–543, May 2009. https://doi.org/10.1111/j.1945-5100.2009.tb00749.x.

V. Bourrier, X. Dumusque, C. Dorn, G. W. Henry, N. Astudillo-Defru, J. Rey, B. Benneke, G. Hébrard, C. Lovis, and B. O. Demory. The 55 Cancri system reassessed. *A&A*, 619:A1, Oct 2018. https://doi.org/10.1051/0004-6361/201833154.

F. Bundy, W. Bassett, M. Weathers, R. Hemley, H. Mao, and A. Goncharov. The pressure-temperature phase and transformation diagram for carbon; updated through 1994. *Carbon*, 34(2):141–153, 1996. ISSN 0008-6223.

F. P. Bundy. Pressure-temperature phase diagram of elemental carbon. *Physica A Statistical Mechanics and its Applications*, 156(1):169–178, Mar 1989. https://doi.org/10.1016/0378-4371(89)90115-5.

A. G. W. Cameron. The partial volatilization of Mercury. *Icarus*, 64(2):285–294, Nov 1985. https://doi.org/10.1016/0019-1035(85)90091-0.

N. L. Chabot, E. A. Wollack, R. L. Klima, and M. E. Minitti. Experimental constraints on Mercury's core composition. *Earth and Planetary Science Letters*, 390: 199–208, Mar 2014. https://doi.org/10.1016/j.epsl.2014.01.004.

J. Cierniewski, A. Karnieli, K. Kuśnierek, A. Goldberg, and I. Herrmann. Approximating the average daily surface albedo with respect to soil roughness and latitude. *International Journal of Remote Sensing*, 34(9-10): 3416–3424, May 2013. https://doi.org/10.1080/01431161.2012.716530.

A. A. Correa, S. A. Bonev, and G. Galli. Carbon under extreme conditions: Phase boundaries and electronic properties from first-principles theory. *Proceedings of the National Academy of Science*, 103:1204–1208, Jan. 2006. https://doi.org/10.1073/pnas.0510489103.

CRC Handbook. *CRC Handbook of Chemistry and Physics, 92nd Edition*. 92 edition, Jun 2011. ISBN 1439855110.

F. Dai, K. Masuda, J. N. Winn, and L. Zeng. Homogeneous Analysis of Hot Earths: Masses, Sizes, and Compositions. *ApJ*, 883(1):79, Sep 2019. https://doi.org/10.3847/1538-4357/ab3a3b.

R. B. Davies and D. S. Harte. Tests for hurst effect. *Biometrika*, 74(1):95–101, 1987. ISSN 00063444.

G. A. de Wijs, G. Kresse, L. Vočadlo, D. Dobson, D. Alfè, M. J. Gillan, and G. D. Price. The viscosity of liquid iron at the physical conditions of the Earth's core. *Nature*, 392(6678):805–807, Apr. 1998. https://doi.org/10.1038/33905.

A. Deliège, T. Kleyntssens, and S. Nicolay. Mars topography investigated through the wavelet leaders method: A multidimensional study of its fractal structure. *Planet. Space Sci.*, 136:46–58, Feb 2017. https://doi.org/10.1016/j.pss.2016.12.008.

S. A. Demin, A. O. Andreev, N. Y. Demina, and Y. A. Nefedyev. The fractal analysis of the gravitational field and topography of the Mars. In *Journal of Physics Conference Series*, volume 929, page 012002, Nov 2017. https://doi.org/10.1088/1742-6596/929/1/012002.

S. A. Demin, A. O. Andreev, N. Y. Demina, and Y. A. Nefedyev. The fractal analysis of the topography and gravitational field of Venus. In *Journal of Physics Conference Series*, volume 1038, page 012020, Jun 2018. https://doi.org/10.1088/1742-6596/1038/1/012020.

B.-O. Demory. The Albedos of Kepler's Close-in Super-Earths. *ApJL*, 789:L20, July 2014. https://doi.org/10.1088/2041-8205/789/1/L20.

D. B. Dingwell, P. Courtial, D. Giordano, and A. R. L. Nichols. Viscosity of peridotite liquid. *Earth and Planetary Science Letters*, 226(1-2):127–138, Sept. 2004. https://doi.org/10.1016/j.epsl.2004.07.017.

A. B. Djurišić and E. H. Li. Optical properties of graphite. *Journal of Applied Physics*, 85(10):7404–7410, May 1999. https://doi.org/10.1063/1.369370.

C. Dorn, J. Venturini, A. Khan, K. Heng, Y. Alibert, R. Helled, A. Rivoldini, and W. Benz. A generalized Bayesian inference method for constraining the interiors of super Earths and sub-Neptunes. *A&A*, 597:A37, Jan. 2017. https://doi.org/10.1051/0004-6361/201628708.

J. Dostal and W. Mueller. *Komatiite Geochemistry*, volume 12, pages 290–298. 01 2004.

X. Dumusque, A. S. Bonomo, R. D. Haywood, L. Malavolta, D. Ségransan, L. A. Buchhave, A. Collier Cameron, D. W. Latham, E. Molinari, and F. Pepe. The Kepler-10 Planetary System Revisited by HARPS-N: A Hot Rocky World and a Solid Neptune-Mass Planet. *ApJ*, 789(2):154, Jul 2014. https://doi.org/10.1088/0004-637X/789/2/154.

P. Durst, G. Mason, B. McKinley, and A. Baylot. Predicting RMS surface roughness using fractal dimension and PSD parameters. *Journal of Terramechanics*, 48(2):105 – 111, Apr 2011. https://doi.org/https://doi.org/10.1016/j.jterra.2010.05.004.

K. S. Edgett and J. Rice, J. W. Geologic Signature of Life on Mars: Low-Albedo Lava Flows and the Search for "Warm Havens". In S. M. Clifford, A. H. Treiman, H. E. Newsom, and J. D. Farmer, editors, *Early Mars: Geologic and Hydrologic Evolution, Physical and Chemical Environments, and the Implications for Life*, volume 916, page 29, Jan. 1997.

W. G. Egan, T. Hilgeman, and K. Pang. Ultraviolet Complex Refractive Index of Martian Dust: Laboratory Measurements of Terrestrial Analogs. *Icarus*, 25(2): 344–355, Jun 1975. https://doi.org/10.1016/0019-1035(75)90029-9.

D. Ehrenreich and J.-M. Désert. Mass-loss rates for transiting exoplanets. *A&A*, 529:A136, May 2011. https://doi.org/10.1051/0004-6361/201016356.

L. T. Elkins-Tanton and S. Seager. Coreless Terrestrial Exoplanets. *ApJ*, 688(1):628–635, Nov 2008. https://doi.org/10.1086/592316.

K. A. Emanuel. *Atmospheric Convection*. Oxford University Press, 1994.

Z. Essack, S. Seager, and M. Pajusalu. Low-albedo Surfaces of Lava Worlds. *ApJ*, 898(2):160, Aug. 2020. https://doi.org/10.3847/1538-4357/ab9cba.

L. J. Esteves, E. J. W. De Mooij, and R. Jayawardhana. Changing Phases of Alien Worlds: Probing Atmospheres of Kepler Planets with High-precision Photometry. *ApJ*, 804(2):150, May 2015. https://doi.org/10.1088/0004-637X/804/2/150.

L. J. Esteves, E. J. W. de Mooij, R. Jayawardhana, C. Watson, and R. de Kok. A Search for Water in a Super-Earth Atmosphere: High-resolution Optical Spectroscopy of 55Cancri e. *AJ*, 153:268, June 2017. https://doi.org/10.3847/1538-3881/aa7133.

L. G. Evans, P. N. Peplowski, E. A. Rhodes, D. J. Lawrence, T. J. McCoy, L. R. Nittler, S. C. Solomon, A. L. Sprague, K. R. Stockstill-Cahill, R. D. Starr, S. Z. Weider, W. V. Boynton, D. K. Hamara, and J. O. Goldsten. Major-element abundances on the surface of Mercury: Results from the MESSENGER Gamma-Ray Spectrometer. *Journal of Geophysical Research (Planets)*, 117:E00L07, Nov 2012. https://doi.org/10.1029/2012JE004178.

D. Fabian, T. Henning, C. Jäger, H. Mutschke, J. Dorschner, and O. Wehrhan. Steps toward interstellar silicate mineralogy. VI. Dependence of crystalline olivine IR spectra on iron content and particle shape. *A&A*, 378:228–238, Oct 2001. https://doi.org/10.1051/0004-6361:20011196.

M. B. Fairbairn. Planetary Photometry: The Lommel-Seeliger Law. *JRASC*, 99(3):92, June 2005.

B. Fegley and L. Schaefer. Silicate Atmosphere and Clouds of Hot Earth-like Exoplanets. *Meteoritics and Planetary Science Supplement*, 72:5032, Sep 2009.

A. Fogtmann-Schulz, B. Hinrup, V. Van Eylen, J. Christensen-Dalsgaard, H. Kjeldsen, V. Silva Aguirre, and B. o. Tingley. Accurate Parameters of the Oldest Known Rocky-exoplanet Hosting System: Kepler-10 Revisited. *ApJ*, 781(2):67, Feb 2014. https://doi.org/10.1088/0004-637X/781/2/67.

S. Fornasier, C. Lantz, D. Perna, H. Campins, M. A. Barucci, and D. Nesvorny. Spectral variability on primitive asteroids of the Themis and Beagle families: Space weathering effects or parent body heterogeneity? *Icarus*, 269:1–14, May 2016. https://doi.org/10.1016/j.icarus.2016.01.002.

G. S. Fulcher. Analysis of recent measurements of the viscosity of glasses: I. *Journal of the American Ceramic Society*, 8(6):339–355, 1925a. https://doi.org/10.1111/j.1151-2916.1925.tb16731.x. URL https://ceramics.onlinelibrary.wiley.com/doi/abs/10.1111/j.1151-2916.1925.tb16731.x.

G. S. Fulcher. Analysis of recent measurements of the viscosity of glasses: Ii. *Journal of the American Ceramic Society*, 8(12):789–794, 1925b. https://doi.org/10.1111/j.1151-2916.1925.tb18582.x. URL https://ceramics.onlinelibrary.wiley.com/doi/abs/10.1111/j.1151-2916.1925.tb18582.x.

B. J. Fulton, E. A. Petigura, A. W. Howard, H. Isaacson, G. W. Marcy, P. A. Cargile, L. Hebb, L. M. Weiss, J. A. Johnson, T. D. Morton, E. Sinukoff, I. J. M. Crossfield, and L. A. Hirsch. The California-Kepler Survey. III. A Gap in the Radius Distribution of Small Planets. *AJ*, 154:109, Sept. 2017. https://doi.org/10.3847/1538-3881/aa80eb.

G. Ghosh. Dispersion-equation coefficients for the refractive index and birefringence of calcite and quartz crystals. *Optics Communications*, 163(1-3):95–102, May 1999. https://doi.org/10.1016/S0030-4018(99)00091-7.

D. Giordano, J. K. Russell, and D. B. Dingwell. Viscosity of magmatic liquids: A model. *Earth and Planetary Science Letters*, 271(1-4):123–134, July 2008. https://doi.org/10.1016/j.epsl.2008.03.038.

D. Grainger, D. Peters, L. Clarisse, and H. Herbin. Aerosol refractive index archive, 2014. URL http://eodg.atm.ox.ac.uk/ARIA/.

H.-J. Hagemann, W. Gudat, and C. Kunz. Optical constants from the far infrared to the x-ray region: Mg, al, cu, ag, au, bi, c, and al2o3. *J. Opt. Soc. Am.*, 65(6): 742–744, Jun 1975. https://doi.org/10.1364/JOSA.65.000742. URL http://www.osapublishing.org/abstract.cfm?URI=josa-65-6-742.

K. Hakim, W. van Westrenen, and C. Dominik. Capturing the oxidation of silicon carbide in rocky exoplanetary interiors. *A&A*, 618:L6, Oct 2018. https://doi.org/10.1051/0004-6361/201833942.

K. Hakim, R. Spaargaren, D. S. Grewal, A. Rohrbach, J. Berndt, C. Dominik, and W. van Westrenen. Mineralogy, Structure, and Habitability of Carbon-Enriched Rocky Exoplanets: A Laboratory Approach. *Astrobiology*, 19(7):867–884, Jul 2019. https://doi.org/10.1089/ast.2018.1930.

V. I. Haltrin, W. E. McBride III, and R. A. Arnone. Spectral approach to calculate specular reflection of light from wavy water surface. pages 133–138, 2001.

K. Hamano, H. Kawahara, Y. Abe, M. Onishi, and G. L. Hashimoto. Lifetime and Spectral Evolution of a Magma Ocean with a Steam Atmosphere: Its Detectability by Future Direct Imaging. *ApJ*, 806(2):216, Jun 2015. https://doi.org/10.1088/0004-637X/806/2/216.

B. Hapke. *Theory of Reflectance and Emittance Spectroscopy*. Cambridge University Press, 2 edition, 2012. https://doi.org/10.1017/CBO9781139025683.

S. A. Hauck, J.-L. Margot, S. C. Solomon, R. J. Phillips, C. L. Johnson, F. G. Lemoine, E. Mazarico, T. J. McCoy, S. Padovan, S. J. Peale, M. E. Perry, D. E. Smith, and M. T. Zuber. The curious case of Mercury's internal structure. *Journal of Geophysical Research (Planets)*, 118(6):1204–1220, Jun 2013. https://doi.org/10.1002/jgre.20091.

D. R. Haughton, P. L. Roeder, and B. J. Skinner. Solubility of Sulfur in Mafic Magmas. *Economic Geology*, 69(4):451–467, 07 1974. ISSN 0361-0128. https://doi.org/10.2113/gsecongeo.69.4.451. URL https://doi.org/10.2113/gsecongeo.69.4.451.

T. Henning, B. Begemann, H. Mutschke, and J. Dorschner. Optical properties of oxide dust grains. *A&AS*, 112:143, Jul 1995.

P. Hoppe, J. Leitner, E. Gröner, K. K. Marhas, B. S. Meyer, and S. Amari. NanoSIMS Studies of Small Presolar SiC Grains: New Insights into Supernova Nucleosynthesis, Chemistry, and Dust Formation. *ApJ*, 719(2):1370–1384, Aug 2010. https://doi.org/10.1088/0004-637X/719/2/1370.

R. Hu, B. L. Ehlmann, and S. Seager. Theoretical Spectra of Terrestrial Exoplanet Surfaces. *ApJ*, 752(1):7, Jun 2012. https://doi.org/10.1088/0004-637X/752/1/7.

D. M. Hunten, R. O. Pepin, and J. C. G. Walker. Mass fractionation in hydrodynamic escape. *Icarus*, 69: 532–549, Mar. 1987. https://doi.org/10.1016/0019-1035(87)90022-4.

Y. Ito, M. Ikoma, H. Kawahara, H. Nagahara, Y. Kawashima, and T. Nakamoto. Theoretical Emission Spectra of Atmospheres of Hot Rocky Super-Earths. *ApJ*, 801(2):144, Mar 2015. https://doi.org/10.1088/0004-637X/801/2/144.

C. Jaeger, F. J. Molster, J. Dorschner, T. Henning, H. Mutschke, and L. B. F. M. Waters. Steps toward interstellar silicate mineralogy. IV. The crystalline revolution. *A&A*, 339:904–916, Nov 1998.

M. Javoy, E. Kaminski, F. Guyot, D. Andrault, C. Sanloup, M. Moreira, S. Labrosse, A. Jambon, P. Agrinier, A. Davaille, and C. Jaupart. The chemical composition of the Earth: Enstatite chondrite models. *Earth and Planetary Science Letters*, 293(3-4):259–268, May 2010. https://doi.org/10.1016/j.epsl.2010.02.033.

S. Jin and C. Mordasini. Compositional Imprints in Density-Distance-Time: A Rocky Composition for Close-in Low-mass Exoplanets from the Location of the Valley of Evaporation. *ApJ*, 853(2):163, Feb 2018. https://doi.org/10.3847/1538-4357/aa9f1e.

S. Jin, C. Mordasini, V. Parmentier, R. van Boekel, T. Henning, and J. Ji. Planetary Population Synthesis Coupled with Atmospheric Escape: A Statistical View of Evaporation. *ApJ*, 795:65, Nov. 2014. https://doi.org/10.1088/0004-637X/795/1/65.

J. Kischkat, S. Peters, B. Gruska, M. Semtsiv, M. Chashnikova, M. Klinkmüller, O. Fedosenko, S. Machulik, A. Aleksandrova, G. Monastyrskyi, Y. Flores, and W. T. Masselink. Mid-infrared optical properties of thin films of aluminum oxide, titanium dioxide, silicon dioxide, aluminum nitride, and silicon nitride. *Appl. Opt.*, 51(28):6789–6798, Oct 2012. https://doi.org/10.1364/AO.51.006789. URL http://ao.osa.org/abstract.cfm?URI=ao-51-28-6789.

E. S. Kite, B. Fegley, Jr., L. Schaefer, and E. Gaidos. Atmosphere-interior Exchange on Hot, Rocky Exoplanets. *ApJ*, 828:80, Sept. 2016. https://doi.org/10.3847/0004-637X/828/2/80.

D. Kubyshkina, L. Fossati, N. V. Erkaev, C. P. Johnstone, P. E. Cubillos, K. G. Kislyakova, H. Lammer, M. Lendl, and P. Odert. Grid of upper atmosphere models for 1-40 $M_\oplus$ planets: application to CoRoT-7 b and HD 219134 b,c. *A&A*, 619:A151, Nov. 2018. https://doi.org/10.1051/0004-6361/201833737.

A. B. Kuzmenko, E. van Heumen, F. Carbone, and D. van der Marel. Universal Optical Conductance of Graphite. *PhRvL*, 100(11):117401, Mar 2008. https://doi.org/10.1103/PhysRevLett.100.117401.

H. Lammer, N. V. Erkaev, P. Odert, K. G. Kislyakova, M. Leitzinger, and M. L. Khodachenko. Probing the blow-off criteria of hydrogen-rich 'super-Earths'. *MNRAS*, 430:1247–1256, Apr. 2013. https://doi.org/10.1093/mnras/sts705.

I. Lazányi and L. Szirmay-Kalos. Fresnel term approximations for metals. In *WSCG'2005: Short Papers Proceedings*, pages 77–80, University of West Bohemia, Plzen, Czech Republic, 01 2005. University of West Bohemia.

R. Le Maitre, A. Streckeisen, B. Zanettin, M. Le Bas, B. Bonin, and P. Bateman. *Igneous Rocks: A Classification and Glossary of Terms: Recommendations of the International Union of Geological Sciences Subcommission on the Systematics of Igneous Rocks*. Cambridge University Press, 2 edition, 2002. https://doi.org/10.1017/CBO9780511535581.

A. Lecavelier Des Etangs. A diagram to determine the evaporation status of extrasolar planets. *A&A*, 461: 1185–1193, Jan. 2007. https://doi.org/10.1051/0004-6361:20065014.

J. S. Lewis. Metal/silicate fractionation in the Solar System. *Earth and Planetary Science Letters*, 15(3): 286–290, Jul 1972. https://doi.org/10.1016/0012-821X(72)90174-4.

J. S. Lewis. The Temperature Gradient in the Solar Nebula. *Science*, 186(4162):440–443, Nov 1974. https://doi.org/10.1126/science.186.4162.440.

S. Lhermitte, J. Abermann, and C. Kinnard. Albedo over rough snow and ice surfaces. *The Cryosphere*, 8(3): 1069–1086, Jun 2014. https://doi.org/10.5194/tc-8-1069-2014.

H. H. Li. Refractive index of silicon and germanium and its wavelength and temperature derivatives. *Journal of Physical and Chemical Reference Data*, 9(3):561–658, Jul 1980. https://doi.org/10.1063/1.555624.

C. J. Liu and E. F. Sieckmann. Refractive Index of Calcium Oxide. *Journal of Applied Physics*, 37(6): 2450–2452, May 1966. https://doi.org/10.1063/1.1708835.

D. Locci, C. Cecchi-Pestellini, and G. Micela. Photo-evaporation of close-in gas giants orbiting around G and M stars. *A&A*, 624:A101, Apr 2019. https://doi.org/10.1051/0004-6361/201834491.

K. Lodders and J. Fegley, B. The origin of circumstellar silicon carbide grains found in meteorites. *Meteoritics*, 30(6):661, Nov 1995. https://doi.org/10.1111/j.1945-5100.1995.tb01164.x.

E. D. Lopez. Born dry in the photoevaporation desert: Kepler's ultra-short-period planets formed water-poor. *MNRAS*, 472(1):245–253, Nov. 2017. https://doi.org/10.1093/mnras/stx1558.

R. D. Lorenz and A. G. Hayes. The growth of wind-waves in Titan's hydrocarbon seas. *Icarus*, 219(1):468–475, May 2012. https://doi.org/10.1016/j.icarus.2012.03.002.

R. Luger and R. Barnes. Extreme Water Loss and Abiotic O_2 Buildup On Planets Throughout the Habitable Zones of M Dwarfs. In *American Astronomical Society Meeting Abstracts #225*, volume 225 of *American Astronomical Society Meeting Abstracts*, page 407.04, Jan 2015.

N. Madhusudhan, K. K. M. Lee, and O. Mousis. A Possible Carbon-rich Interior in Super-Earth 55 Cancri e. *ApJ*, 759(2):L40, Nov 2012. https://doi.org/10.1088/2041-8205/759/2/L40.

G. Mahapatra, C. Helling, and Y. Miguel. Cloud formation in metal-rich atmospheres of hot super-Earths like 55 Cnc e and CoRoT7b. *MNRAS*, 472(1):447–464, Nov 2017. https://doi.org/10.1093/mnras/stx1666.

V. Malavergne, M. J. Toplis, S. Berthet, and J. Jones. Highly reducing conditions during core formation on Mercury: Implications for internal structure and the origin of a magnetic field. *Icarus*, 206(1):199–209, Mar 2010. https://doi.org/10.1016/j.icarus.2009.09.001.

V. Malavergne, P. Cordier, K. Righter, F. Brunet, B. Zanda, A. Addad, T. Smith, H. Bureau, S. Surblé, C. Raepsaet, E. Charon, and R. H. Hewins. How Mercury can be the most reduced terrestrial planet and still store iron in its mantle. *Earth and Planetary Science Letters*, 394:186–197, May 2014. https://doi.org/10.1016/j.epsl.2014.03.028.

L. Malavolta. Ultra-short Period Rocky Super-Earths. *European Planetary Science Congress*, 12: EPSC2018-1115, Sept. 2018.

B. Malyuk. Major-element series and types of komatiites. *All-Union Institute of Scientific and Technical Information, Moscow*, 37:16–12, 12 1986.

B. B. Mandelbrot. Stochastic Models for the Earth's Relief, the Shape and the Fractal Dimension of the Coastlines, and the Number-Area Rule for Islands. *Proceedings of the National Academy of Science*, 72(10):3825–3828, Oct 1975. https://doi.org/10.1073/pnas.72.10.3825.

R. A. Marcus, D. Sasselov, L. Hernquist, and S. T. Stewart. Minimum Radii of Super-Earths: Constraints from Giant Impacts. *ApJL*, 712(1):L73–L76, Mar 2010. https://doi.org/10.1088/2041-8205/712/1/L73.

M. S. Marley, C. Gelino, D. Stephens, J. I. Lunine, and R. Freedman. Reflected Spectra and Albedos of Extrasolar Giant Planets. I. Clear and Cloudy Atmospheres. *ApJ*, 513(2):879–893, Mar. 1999. https://doi.org/10.1086/306881.

A. D. Matthias, A. Fimbres, E. E. Sano, D. F. Post, L. Accioly, A. K. Batchily, and L. G. Ferreira. Surface Roughness Effects on Soil Albedo. *Soil Science Society of America Journal*, 64(3):1035, Jan 2000. https://doi.org/10.2136/sssaj2000.6431035x.

T. J. McCoy, T. L. Dickinson, and G. E. Lofgren. Partial melting of the Indarch (EH4) Meteorite: A textural, chemical and phase relations view of melting and melt migration. *Meteoritics and Planetary Science*, 34(5): 735–746, Sep 1999. https://doi.org/10.1111/j.1945-5100.1999.tb01386.x.

Met Office. National Meteorological Library and Archive Fact Sheet 6 - The Beaufort Scale, Mar 2010. URL https://www.metoffice.gov.uk/binaries/content/assets/metofficegovuk/pdf/research/library-and-archive/library/publications/factsheets/factsheet_6-the-beaufort-scale.pdf.

F. Miozzi, G. Morard, D. Antonangeli, A. N. Clark, M. Mezouar, C. Dorn, A. Rozel, and G. Fiquet. Equation of State of SiC at Extreme Conditions: New Insight Into the Interior of Carbon-Rich Exoplanets. *Journal of Geophysical Research (Planets)*, 123(9):2295–2309, Sep 2018. https://doi.org/10.1029/2018JE005582.

D. Modirrousta-Galian, D. Locci, and G. Micela. The bimodal distribution in exoplanet radii: Considering varying core compositions and h2 envelope's sizes. *The Astrophysical Journal*, 891(2):158, mar 2020a. https://doi.org/10.3847/1538-4357/ab7379. URL https://doi.org/10.3847%2F1538-4357%2Fab7379.

D. Modirrousta-Galian, D. Locci, G. Tinetti, and G. Micela. Hot super-earths with hydrogen atmospheres: A model explaining their paradoxical existence. *The Astrophysical Journal*, 888(2):87, jan 2020b. https://doi.org/10.3847/1538-4357/ab616b. URL https://doi.org/10.3847%2F1538-4357%2Fab616b.

J. Moriarty, N. Madhusudhan, and D. Fischer. Chemistry in an Evolving Protoplanetary Disk: Effects on Terrestrial Planet Composition. *ApJ*, 787(1):81, May 2014. https://doi.org/10.1088/0004-637X/787/1/81.

O. Namur, B. Charlier, F. Holtz, C. Cartier, and C. McCammon. Sulfur solubility in reduced mafic silicate melts: Implications for the speciation and distribution of sulfur on Mercury. *Earth and Planetary Science Letters*, 448:102–114, Aug 2016. https://doi.org/10.1016/j.epsl.2016.05.024.

L. R. Nittler and S. Z. Weider. The Surface Composition of Mercury. *Elements*, 15(1):33–38, 02 2019. ISSN 1811-5209. https://doi.org/10.2138/gselements.15.1.33. URL https://doi.org/10.2138/gselements.15.1.33.

L. R. Nittler, R. D. Starr, S. Z. Weider, T. J. McCoy, W. V. Boynton, D. S. Ebel, C. M. Ernst, L. G. Evans, J. O. Goldsten, D. K. Hamara, D. J. Lawrence, R. L. McNutt, C. E. Schlemm, S. C. Solomon, and A. L. Sprague. The Major-Element Composition of Mercury's Surface from MESSENGER X-ray Spectrometry. *Science*, 333(6051): 1847, Sep 2011. https://doi.org/10.1126/science.1211567.

P. Oguntunde, A. Ajayi, and N. van de Giesen. Tillage and surface moisture effects on bare-soil albedo of a tropical loamy
sand. *Soil and Tillage Research*, 85(1):107 – 114, Jan 2006. https://doi.org/https://doi.org/10.1016/j.still.2004.12.009. URL http://www.sciencedirect.com/science/article/pii/S0167198705000462.

H. S. C. O'Neill and H. Palme. Composition of the silicate earth: implications for accretion of and core formation. In I. Jackson, editor, *The Earth's mantle; composition, structure, and evolution*, volume 264, pages 3–126, Cambridge, 1998. Cambridge University Press.

M. A. Ordal, R. J. Bell, J. Alexander, Ralph W., L. A. Newquist, and M. R. Querry. Optical properties of Al, Fe, Ti, Ta, W, and Mo at submillimeter wavelengths. *ApOpt*, 27(6):1203–1209, Mar 1988. https://doi.org/10.1364/AO.27.001203.

J. E. Owen and Y. Wu. Kepler Planets: A Tale of Evaporation. *ApJ*, 775:105, Oct. 2013. https://doi.org/10.1088/0004-637X/775/2/105.

J. E. Owen and Y. Wu. The Evaporation Valley in the Kepler Planets. *ApJ*, 847:29, Sept. 2017. https://doi.org/10.3847/1538-4357/aa890a.

R. J. Papoular and R. Papoular. Some optical properties of graphite from IR to millimetric wavelengths. *MNRAS*, 443(4):2974–2982, Oct 2014. https://doi.org/10.1093/mnras/stu1348.

H. R. Philipp. Infrared optical properties of graphite. *PhRvB*, 16(6):2896–2900, Sep 1977. https://doi.org/10.1103/PhysRevB.16.2896.

W. Pluriel, E. Marcq, and M. Turbet. Modeling the albedo of Earth-like magma ocean planets with H_2O-CO_2 atmospheres. *Icarus*, 317:583–590, Jan 2019. https://doi.org/10.1016/j.icarus.2018.08.023.

J. B. Pollack, O. B. Toon, and B. N. Khare. Optical properties of some terrestrial rocks and glasses. *Icarus*, 19(3):372–389, Jul 1973. https://doi.org/10.1016/0019-1035(73)90115-2.

M. N. Polyanskiy. Refractive index database, 2010. URL https://refractiveindex.info.

T. Posch, A. Baier, H. Mutschke, and T. Henning. Carbonates in Space: The Challenge of Low-Temperature Data. *ApJ*, 668(2):993–1000, Oct 2007. https://doi.org/10.1086/521390.

M. R. Querry. Optical constants. Technical report, Jun 1985.

M. R. Querry. *Optical Constants of Minerals and Other Materials from the Millimeter to the Ultraviolet*. PhD thesis, University of Missouri-Kansas City, 1987.

A. D. Rakić and M. L. Majewski. Modeling the optical dielectric function of GaAs and AlAs: Extension of Adachi's model. *Journal of Applied Physics*, 80(10): 5909–5914, Nov 1996. https://doi.org/10.1063/1.363586.

A. D. Rakić, A. B. Djurišić, J. M. Elazar, and M. L. Majewski. Optical properties of metallic films for vertical-cavity optoelectronic devices. *Appl. Opt.*, 37(22): 5271–5283, Aug 1998. https://doi.org/10.1364/AO.37.005271. URL http://ao.osa.org/abstract.cfm?URI=ao-37-22-5271.

A. R. Ridden-Harper, I. A. G. Snellen, C. U. Keller, R. J. de Kok, E. Di Gloria, H. J. Hoeijmakers, M. Brogi, M. Fridlund, B. L. A. Vermeersen, and W. van Westrenen. Search for an exosphere in sodium and calcium in the transmission spectrum of exoplanet 55 Cancri e. *A&A*, 593:A129, Oct. 2016. https://doi.org/10.1051/0004-6361/201628448.

M. A. Riner, C. R. Bina, M. S. Robinson, and S. J. Desch. Internal structure of Mercury: Implications of a molten core. *Journal of Geophysical Research (Planets)*, 113 (E8):E08013, Aug 2008. https://doi.org/10.1029/2007JE002993.

D. Rouan, H. J. Deeg, O. Demangeon, B. Samuel, C. Cavarroc, B. Fegley, and A. Léger. The Orbital Phases and Secondary Transits of Kepler-10b. A Physical Interpretation Based on the Lava-ocean Planet Model. *ApJL*, 741(2):L30, Nov 2011. https://doi.org/10.1088/2041-8205/741/2/L30.

J. K. Russell, D. Giordano, and D. B. Dingwell. High-temperature limits on viscosity of non-Arrhenian silicate melts. *American Mineralogist*, 88(8-9):1390–1394, Aug. 2004. https://doi.org/10.2138/am-2003-8-924.

L. Schaefer and B. Fegley. Chemistry of Silicate Atmospheres of Evaporating Super-Earths. *ApJL*, 703: L113–L117, Oct. 2009. https://doi.org/10.1088/0004-637X/703/2/L113.

L. Schaefer, K. Lodders, and B. Fegley. Vaporization of the Earth: Application to Exoplanet Atmospheres. *ApJ*, 755: 41, Aug. 2012. https://doi.org/10.1088/0004-637X/755/1/41.

C. Schlick. An inexpensive brdf model for physically-based rendering. *Computer Graphics Forum*, 13(3):233–246, 1994. https://doi.org/10.1111/1467-8659.1330233.

H. Seeliger. Zur photometrie des saturnringes. *Astronomische Nachrichten*, 109(20):305–314, 1884. https://doi.org/10.1002/asna.18841092002. URL https://onlinelibrary.wiley.com/doi/abs/10.1002/asna.18841092002.

M. Shelberg, N. Lam, and H. Moellering. Measuring the fractal dimensions of surfaces. page 11, 10 1983.

D. I. Shestopalov, L. F. Golubeva, and E. A. Cloutis. Optical maturation of asteroid surfaces. *Icarus*, 225(1): 781–793, Jul 2013. https://doi.org/10.1016/j.icarus.2013.05.002.

T. Siefke, S. Kroker, K. Pfeiffer, O. Puffky, K. Dietrich, D. Franta, I. Ohlídal, A. Szeghalmi, E.-B. Kley, and A. Tünnermann. Materials pushing the application limits of wire grid polarizers further into the deep ultraviolet spectral range. *Advanced Optical Materials*, 4 (11):1780–1786, 2016. https://doi.org/10.1002/adom.201600250. URL https://onlinelibrary.wiley.com/doi/abs/10.1002/adom.201600250.

R. E. Stephens and I. H. Malitson. Index of Refraction of Magnesium Oxide. *Journal of Research of the National Bureau of Standards*, 49(4):249–252, Oct 1952.

M. Stiassnie. The fractal dimension of the ocean surface. pages 633–647, 01 1991.

M. Stiassnie, Y. Agnon, and L. Shemer. Fractal dimensions of random water surfaces. *Physica D Nonlinear Phenomena*, 47(3):341–352, Jan 1991. https://doi.org/10.1016/0167-2789(91)90034-7.

M. R. Swain, R. Estrela, C. Sotin, G. M. Roudier, and R. T. Zellem. Two Terrestrial Planet Families with Different Origins. *ApJ*, 881(2):117, Aug 2019. https://doi.org/10.3847/1538-4357/ab2714.

E. A. Taft and H. R. Philipp. Optical Properties of Graphite. *Physical Review*, 138(1A):197–202, Apr 1965. https://doi.org/10.1103/PhysRev.138.A197.

G. Tammann and W. Hesse. Die abhängigkeit der viscosität von der temperatur bie unterkühlten flüssigkeiten. *Zeitschrift für anorganische und allgemeine Chemie*, 156(1):245–257, 1926. https://doi.org/10.1002/zaac.19261560121. URL https://onlinelibrary.wiley.com/doi/abs/10.1002/zaac.19261560121.

A. Tsiaras, M. Rocchetto, I. P. Waldmann, O. Venot, R. Varley, G. Morello, M. Damiano, G. Tinetti, E. J. Barton, S. N. Yurchenko, and J. Tennyson. Detection of an Atmosphere Around the Super-Earth 55 Cancri e. *ApJ*, 820:99, Apr. 2016. https://doi.org/10.3847/0004-637X/820/2/99.

D. Valencia, T. Guillot, V. Parmentier, and R. S. Freedman. Bulk Composition of GJ 1214b and Other Sub-Neptune Exoplanets. *ApJ*, 775:10, Sept. 2013. https://doi.org/10.1088/0004-637X/775/1/10.

D. Viswanath and G. Natarajan. *Data Book on the Viscosity of Liquids*. Hemisphere Publishing Corporation, 1989. ISBN 0-89116-778-1.

H. Vogel. Das Temperaturabhängigkeitsgesetz der Viskosität von Flüssigkeiten. *Physikalische Zeitschrift*, 22(28):645–646, 1921.

S. Wang, M. Zhan, G. Wang, H. Xuan, W. Zhang, C. Liu, C. Xu, Y. Liu, Z. Wei, and X. Chen. 4H-SiC: a new nonlinear material for midinfrared lasers. *Laser & Photonics Review*, 7(5):831–838, Sep 2013. https://doi.org/10.1002/lpor.201300068.

J. T. Wasson and G. W. Kallemeyn. Compositions of Chondrites. *Philosophical Transactions of the Royal Society of London Series A*, 325(1587):535–544, Jul 1988. https://doi.org/10.1098/rsta.1988.0066.

S. Z. Weider, L. R. Nittler, R. D. Starr, T. J. McCoy, and S. C. Solomon. Variations in the abundance of iron on Mercury's surface from MESSENGER X-Ray Spectrometer observations. *Icarus*, 235:170–186, Jun 2014. https://doi.org/10.1016/j.icarus.2014.03.002.

L. M. Weiss, L. A. Rogers, H. T. Isaacson, E. Agol, G. W. Marcy, J. F. Rowe, D. Kipping, B. J. Fulton, J. J. Lissauer, and A. W. Howard. Revised Masses and Densities of the Planets around Kepler-10. *ApJ*, 819(1): 83, Mar 2016. https://doi.org/10.3847/0004-637X/819/1/83.

P. Woitke, C. Helling, G. H. Hunter, J. D. Millard, G. E. Turner, M. Worters, J. Blecic, and J. W. Stock. Equilibrium chemistry down to 100 K. Impact of silicates and phyllosilicates on the carbon to oxygen ratio. *A&A*, 614:A1, Jun 2018. https://doi.org/10.1051/0004-6361/201732193.

A. T. A. Wood and G. Chan. Simulation of stationary gaussian processes in [0,1]d. *Journal of Computational and Graphical Statistics*, 3(4):409–432, 1994.

K. J. Zahnle and J. F. Kasting. Mass fractionation during transonic escape and implications for loss of water from Mars and Venus. *Icarus*, 68(3):462–480, Dec 1986. https://doi.org/10.1016/0019-1035(86)90051-5.

S. Zeidler, T. Posch, H. Mutschke, H. Richter, and O. Wehrhan. Near-infrared absorption properties of oxygen-rich stardust analogs. The influence of coloring metal ions. *A&A*, 526:A68, Feb 2011. https://doi.org/10.1051/0004-6361/201015219.

L. Zeng and D. Sasselov. A Detailed Model Grid for Solid Planets from 0.1 through 100 Earth Masses. *PASP*, 125 (925):227, Mar 2013. https://doi.org/10.1086/669163.

L. Zeng, D. D. Sasselov, and S. B. Jacobsen. Mass-Radius Relation for Rocky Planets Based on PREM. *ApJ*, 819: 127, Mar. 2016. https://doi.org/10.3847/0004-637X/819/2/127.

L. Zeng, S. B. Jacobsen, D. D. Sasselov, A. M. Vand
erburg, M. Lopez-Morales, J. Perez-Mercader, M. I.
Petaev, T. R. Mattsson, G. Li, and H. Matthew. Growth
Model Interpretation of Planet Size Distribution. In
AGU Fall Meeting Abstracts, volume 2018, pages
P53C–2985, Dec 2018.

APPENDIX

A. A COMPARISON OF SCHLICK'S APPROXIMATION WITH OTHER MODELS

Schlick's approximation with a correction for the complex index of refraction matches the Fresnel equations well. This approach has been adopted by other models such as Lazányi and Szirmay-Kalos (2005), who use an *ad hoc* correction to account for the behaviour of the complex refractive index. In spite of this, their model is only applicable for low n and k values. In our model we created n_{sy} in order to account for the effects of the imaginary refractive index (i.e. k) whilst in their paper they added a term to Schlick's approximation which includes k. Having said this, we decided not to use the model by Lazányi and Szirmay-Kalos (2005) as it overestimates the reflectance at small angles of incidence and it becomes inaccurate at high indices of refraction (see Fig. 8). In addition, their model has *ad-hoc* corrections whilst ours is Schlick's approximation with an implementation of the imaginary index of refraction. Our method is slightly more computationally intensive than the one proposed by Lazányi and Szirmay-Kalos (2005) but we believe that it is the appropriate balance of accuracy and efficiency for our purposes.

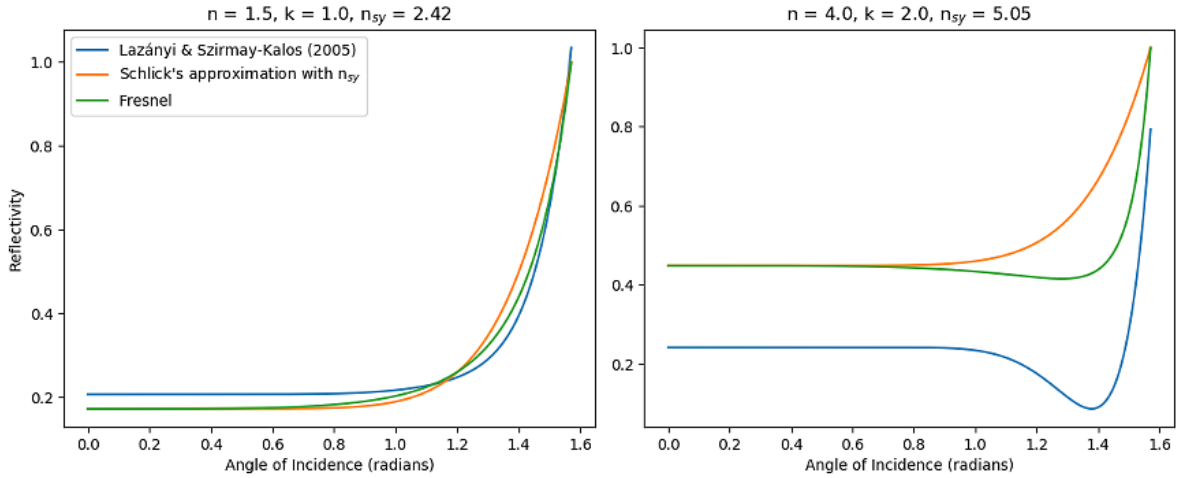

Figure 8. A comparison of the model by Lazányi and Szirmay-Kalos (2005), Schlick's approximation with n_{sy}, and the Fresnel equations.

Another commonly used model for planetary photometry is the Lommel-Seeliger Law (Seeliger 1884). This is a simple analytical approach that well approximates diffuse reflection. Unfortunately, this model fails for spherical albedo values larger than $\simeq 0.20$ (Fairbairn 2005), which falls short of the remit of our study. Another alternative model is the Hapke model (Hapke 2012), which is a semi-empirical analytical approach for estimating the spherical albedo of airless bodies. We decided not to use this method as it is adapted for regolith surfaces such as asteroids, but not fluids like magmas.

In any case, even for unusually high indices of refraction our approach closely matches the results predicted from the Fresnel equations (see Fig. 8) for most angles of incidence. Only at very high angles of incidence do the deviations become noticeable. To further emphasise the suitability of our approach, we ran a ray tracing simulation with $n_{sy} = 6$ and $H = 0.01$ (very rough) with Schlick's approximation and the Fresnel equations to give a spherical albedo of 0.495 and 0.480 respectively. As one can see, the two models provide almost identical results. We are aware that the Fresnel equations are more accurate but we had to make this compromise in order to keep the simulations inexpensive.

B. DERIVATION OF THE SYNTHETIC REFRACTIVE INDEX

From classical electromagnetic theory (Abraham and Becker 1950), the reflectance of a system in contact with a vacuum (or an optically thin medium) is:

$$R = \left(\frac{|n-1|^2 + |k|^2}{|n+1|^2 + |k|^2} \right) \tag{B1a}$$

Table 4. Assumptions used to calculate the Hurst exponent of Kepler-10b

Variable	Approximation	Explanation
Day-side temperature (T_{day})	~ 2750 K	Sub-stellar point temperature for a blackbody.
Mineral atmosphere wind speeds (v_{atm})	$\sim 100\ \mathrm{ms}^{-1}$	This is hard to model and it is not within the objectives of our study so for simplicity we will adopt the values used by Kite et al. (2016).
Mineral atmosphere pressure (P_{atm})	~ 7000 Pa	We used the data from Ito et al. (2015) with a best-fit equation of the form given by Fegley and Schaefer (2009).
Density of magma (ρ_l)	$\sim 2000\ \mathrm{kg\ m}^{-3}$	We adopt the density of an Earth-like rhyolitic magma as at the high temperatures found on Kepler-10b's day-side, relatively low magma densities would be expected.

Let us now define the synthetic refractive index, n_{sy}, as an index which is real and able to reproduce an identical reflectance:

$$R = \left(\frac{n_{sy}-1}{n_{sy}+1}\right)^2 \tag{B1b}$$

Since we have defined n_{sy} as a real index that is able to produce the same reflectance, we can equate Eq. B1a with Eq. B1b:

$$\left(\frac{n_{sy}-1}{n_{sy}+1}\right)^2 = \left(\frac{|n-1|^2+|k|^2}{|n+1|^2+|k|^2}\right) \tag{B1c}$$

Solving for n_{sy} gives:

$$n_{sy} = \frac{\left(\frac{|n-1|^2+|k|^2}{|n+1|^2+|k|^2}\right)^{1/2}+1}{1-\left(\frac{|n-1|^2+|k|^2}{|n+1|^2+|k|^2}\right)^{1/2}} \tag{B1d}$$

C. ESTIMATING THE HURST EXPONENT OF KEPLER-10B

Using the ideal gas equation in conjunction with the data from Table 4, the density of the atmosphere can be estimated at $\sim 6\times10^{-3}\ \mathrm{kg\ m}^{-3}$. Furthermore, using Eq. 1 from Kite et al. (2016), the diameter of the magma ocean is calculated to be approximately $\mathrm{L} \approx 3\times10^{7}$ m. With this information we can now estimate the atmospheric-ocean energy transfer (Lorenz and Hayes 2012; Kite et al. 2016):

$$E \sim \frac{1}{2} C_d \rho_{atm} \varepsilon v_{atm}^2 L \tag{C2}$$

Where $C_d \sim 2\times10^{-3}$ is the equivalent of a drag coefficient (Emanuel 1994) and $\varepsilon \sim 0.01$ is an efficiency factor for winds near the ocean surface (Kite et al. 2016). Inputting the above mentioned data into Eq. C2 gives $\mathrm{E} \sim 2\times10^{4}\ \mathrm{J\ m}^{-2}$. Finally, we can use Eq. 2 from Lorenz and Hayes (2012) to estimate the wave height:

$$E \sim \frac{1}{8} \rho_l g_P h^2 \tag{C3}$$

Where g_P is the gravitational acceleration and h is the wave height. We know that the wave height (peak to trough) is twice the RMS height, and we also know how the RMS is related to the Hurst exponent which is shown in Eq. 4. Therefore, with a few trivial calculations the Hurst exponent can be estimated to be approximately $H \sim 0.8$.

D. SPHERICAL ALBEDO VALUES OF DIFFERENT MATERIALS

Here we show the spherical albedo values for different materials and a constant Hurst exponent of 0.8:

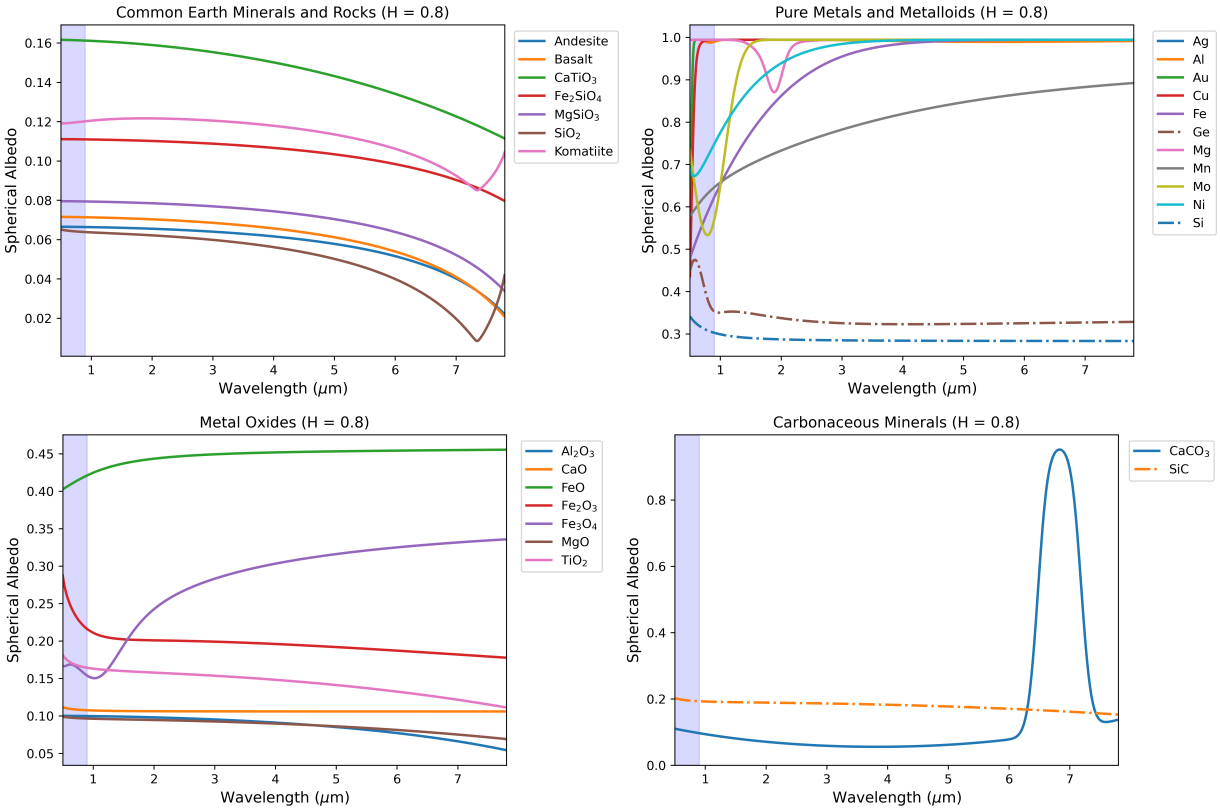

Figure 9. The spherical albedo values of common Earth minerals and rocks, metals and metalloids, metal oxides, and two carbonaceous minerals, for a Hurst exponent of 0.8. The light-blue section is *Kepler's* band-pass. This figure was generated with Eq. (6), (8a), (8b), (9a), and (9b).

E. LIST OF EQUATIONS FOR THE DIFFERENT MATERIALS

Table 5. Best-fit equations for the relationship between the refractive index and the wavelength of light. For komatiite (shown in Fig. 9) we used 9:4:2 of SiO_2, MgO and FeO (Malyuk 1986; Dostal and Mueller 2004).

Material	Best-fit Equation for n, k or n_{sy}	Reference
Ag (n)	$0.0387594 - 0.0191537\lambda + 0.0560141\lambda^2 - 0.000858264\lambda^3$	Babar and Weaver (2015)
Ag (k)	$-0.564253 + 7.70979\lambda - 0.050914\lambda^2$	Babar and Weaver (2015)
Al (n)	$0.312451 + \frac{33.7164\lambda^2}{66.9468+\lambda^2} + \lambda^{6.49463-12.476\lambda^{1.51686}}$	Ordal et al. (1988)
Al (k)	$5.13215 + \frac{9.6749\lambda^2}{1.7134+\lambda^2} + \lambda^{1.4507-2.77918\lambda^{-0.854905}}$	Ordal et al. (1988)
Al_2O_3 (n)	$\left(3.086 + \frac{4.90423\lambda^2}{\lambda^2-307.228}\right)^{1/2}$	Querry (1987)
Al_2O_3 (k)	$\left(0.000319568 - \frac{0.00116775\lambda^2}{\lambda^2-90.2538}\right)^{1/2}$	Querry (1987)
Andesite (n_{sy})	$\left(2.1743 + \frac{0.648257\lambda^2}{\lambda^2-103.233}\right)^{1/2}$	Pollack et al. (1973)
Au (n)	$(0.040181 + 0.010122\lambda + 0.0525666\lambda^2 + 0.000539972\lambda^3 + \frac{0.000157248}{\lambda^{12.1332}}$	Babar and Weaver (2015)
Au (k)	$\left(-10.9924 + 5.09542\lambda + 46.1863\lambda^2\right)^{1/2}$	Babar and Weaver (2015)
Basalt (n_{sy})	$\left(2.298649 - \frac{0.00148953\lambda^2}{\lambda^2+4.37075} + \frac{0.841871\lambda^2}{\lambda^2-108.512}\right)^{1/2}$	Pollack et al. (1973)
$CaCO_3$ (n_{sy})	$1.38352e^{-\frac{(\lambda-3.82577)^2}{-38.7232}} + 23.3249e^{-\frac{(\lambda-6.83304)^2}{0.0826662}}$	Ghosh (1999); Posch et al. (2007)

Table 5. Best-fit equations for the relationship between the refractive index and the wavelength of light. For komatiite (shown in Fig. 9) we used 9:4:2 of SiO_2, MgO and FeO (Malyuk 1986; Dostal and Mueller 2004).

Material	Best-fit Equation for n, k or n_{sy}	Reference
CaO (n_{sy})	$\left(1+\frac{2.260277\lambda^2}{\lambda^2-0.01804729}\right)^{1/2}$	Liu and Sieckmann (1966)
$CaTiO_3$ (n_{sy})	$\left(5.29944+\frac{51.8911\lambda^2}{\lambda^2-1752.85}\right)^{1/2}$	Zeidler et al. (2011)
Cu (n)	$\left(0.0933843+\frac{1098.64\lambda^2}{1727.94+\lambda^2}+\frac{-20.7799\lambda^2}{37.8+\lambda^2}+\frac{0.000030363}{\lambda^{15.601}}\right)^{1/2}$	Babar and Weaver (2015)
Cu (k)	$\left(-5.80213-\frac{13691.8\lambda^2}{-560.774+\lambda^2}+\frac{1097.43\lambda^2}{66.0935+\lambda^2}\right)^{1/2}$	Babar and Weaver (2015)
Fe (n)	$\left(5.8345+\frac{10.4512\lambda^2}{\lambda^2+1.62692}\frac{221.262\lambda^2}{\lambda^2+580.508}\right)^{1/2}$	Querry (1987)
Fe (k)	$\left(1.09676+11.6663\lambda+5.19826\lambda^2+0.256431\lambda^3\right)^{1/2}$	Querry (1987)
FeO (n)	$\left(5.4211+\frac{177291\lambda^2}{\lambda^2+9.98168}-\frac{177290\lambda^2}{\lambda^2+9.9821}\right)^{1/2}$	Henning et al. (1995)
FeO (k)	$\left(5.02746+\frac{2.38467\lambda^2}{0.988753\lambda^2}\right)^{1/2}$	Henning et al. (1995)
Fe_2O_3 (n)	$\left(24.0927-\frac{42.0941\lambda^2}{0.23055+\lambda^2}-\frac{4.66637\lambda^2}{142.27+\lambda^2}+\frac{25.4114\lambda^2}{0.426954+\lambda^2}\right)^{1/2}$	Querry (1987)
Fe_2O_3 (k)	$1.81355-\frac{1.7828}{\lambda^{0.00612776}}+\frac{0.00612776}{\lambda^{6.74851}}$	Querry (1987)
Fe_3O_4 (n)	$\left(191.094-\frac{564.131}{\lambda}+\frac{646.954}{\lambda^2}-\frac{308.721}{\lambda^3}+\frac{52.8087}{\lambda^4}\right)^{0.263078}$	Querry (1987)
Fe_3O_4 (k)	$\left(0.56873+\frac{1.141}{\lambda}-\frac{0.933493}{\lambda^2}-\frac{4.37513}{\lambda^3}+\frac{8.59397}{\lambda^4}\right)^{-0.713551}$	Querry (1987)
Fe_2SiO_4 (n_{sy})	$\left(3.42567+\frac{0.981637\lambda^2}{\lambda^2-125.692}\right)^{1/2}$	Fabian et al. (2001)
GaAs (n)	$\left(14.2857+\frac{1.31107\lambda^2}{\lambda^2-0.19523}+\frac{4266.07\lambda^2}{\lambda^2+1.03145}+\frac{-4270.94\lambda^2}{\lambda^2+1.03024}\right)^{1/2}$	Rakić and Majewski (1996)
GaAs (k)	$10^{\left(-4.13226+\frac{2.44252}{\lambda^{0.678051}}\right)}$	Rakić and Majewski (1996)
Ge (n)	$9.27088-\frac{1}{0.342728\lambda}-\frac{1}{24.1123\lambda^2}-\frac{5.00253\lambda^2}{\lambda^2+1.41971}$	Amotchkina et al. (2020)
Ge (k)	$\frac{1.12327}{(1.01186-0.0522531\lambda+0.0452528\lambda^2)^{290.1425}}$	Amotchkina et al. (2020)
Mg (n)	$\left\lvert-1.48883+2.57035\lambda+0.213623\lambda^{-9.93907\lambda^2+27.2749\lambda-10.8071}\right\rvert$	Hagemann et al. (1975)
Mg (k)	$\left\lvert-3.08158+1.74441\lambda+11.9179\lambda^{-0.000808172\lambda^{13.8785}-542.183\lambda^{0.000433637}+542.183}+\frac{745.947\lambda^2}{1.994+\lambda^2}-\frac{717.65\lambda^2}{1.87182+\lambda^2}\right\rvert$	Hagemann et al. (1975)
MgO (n_{sy})	$\left(2.956362+\frac{0.02195770}{\lambda^2-0.01428322}-0.01062387\lambda^2-0.0000204968\lambda^4\right)^{1/2}$	Stephens and Malitson (1952)
$MgSiO_3$ (n_{sy})	$1.58257+\frac{0.219036\lambda^2}{\lambda^2-96.5198}$	Jaeger et al. (1998)
Mn (n)	$\left(-1.41011+\frac{41.9909\lambda^2}{\lambda^2+2.52168}+\frac{281.743\lambda^2}{\lambda^2+134.924}\right)^{1/2}$	Querry (1987)
Mn (k)	$\left(-0.499692+\frac{95.9185\lambda^2}{47.4233+\lambda^2}+\frac{26.3224\lambda^2}{0.460497+\lambda^2}\right)^{1/2}$	Querry (1987)
Mo (n)	$\left(-74264.2+\frac{74262\lambda^2}{-0.000113513+\lambda^2}+\frac{-40.6174\lambda^2}{-102.076+\lambda^2}\right)^{1/2}$	Ordal et al. (1988)
Mo (k)	$\left(-32.634+\frac{38213\lambda^2}{1092.74+\lambda^2}+\frac{13.6911}{\lambda^2}\right)^{1/2}$	Ordal et al. (1988)
Ni (n)	$\left(-36.2204+\frac{23.8522\lambda^2}{7.4471+\lambda^2}-\frac{9.67652\lambda^2}{\lambda^2-90.5159}+\frac{42.2902\lambda^2}{0.0310738+\lambda^2}\right)^{1/2}$	Rakić et al. (1998)
Ni (k)	$1.74046+3.38213\lambda$	Rakić et al. (1998)
Si (n_{sy})	$\left(1381.62-\frac{1369.35\lambda^2}{\lambda^2+0.000919293}\right)^{1/2}$	Li (1980)
SiC (n_{sy})	$\left(1+\frac{0.20075\lambda^2}{\lambda^2+12.07224}+\frac{5.54861\lambda^2}{\lambda^2-0.02641}+\frac{35.65066\lambda^2}{\lambda^2-1268.24708}\right)^{1/2}$	Wang et al. (2013)
SiO_2 (n)	$\left(1+\frac{0.6961663\lambda^2}{\lambda^2-0.0684043^2}+\frac{0.4079426\lambda^2}{\lambda^2-0.1162414^2}+\frac{0.8974794\lambda^2}{\lambda^2-9.896161^2}\right)^{1/2}$	Kischkat et al. (2012)
SiO_2 (k)	$0.00813575-0.00164212\lambda-\frac{0.00216415\lambda^2}{\lambda^2-62.6425}$	Kischkat et al. (2012)
TiO_2 (n_{sy})	$\left(3.36314+\frac{1.85104\lambda^2}{\lambda^2-0.0852835}-\frac{78.7336\lambda^2}{2617.1+\lambda^2}\right)^{1/2}$	Siefke et al. (2016)

F. ATMOSPHERIC EFFECTS

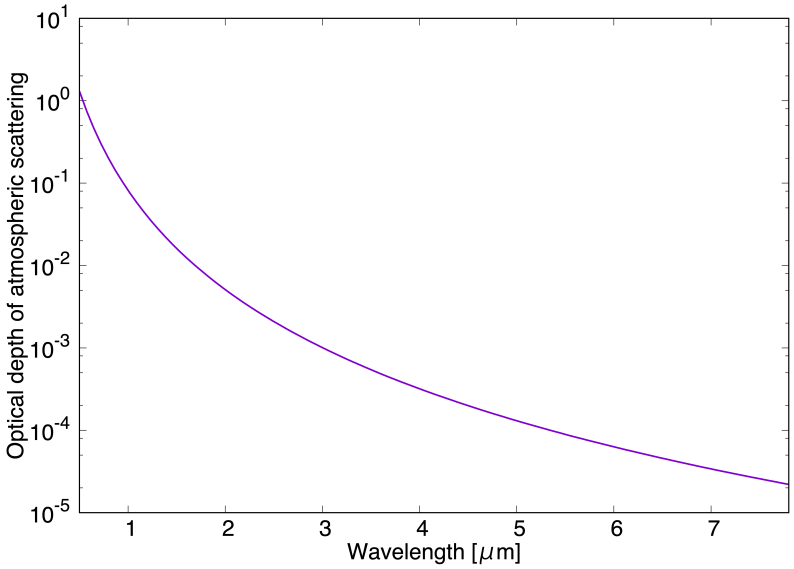

Figure 10. The vertical optical depth of Rayleigh scattering as a function of wavelength for a pure Na atmosphere on Kepler-10b. The optical depth is derived assuming a pressure of 7×10^4 dyne/cm^2, 1700 cm/s^2 as the surface gravity, and Na as the sole atmospheric constituent.